

UC San Diego

UC San Diego Previously Published Works

Title

Control of Bering Strait transport by the meridional overturning circulation
Control of Bering Strait transport by the meridional overturning circulation

Permalink

<https://escholarship.org/uc/item/26w808nv>

Journal

Journal of Physical Oceanography, 50(7)

ISSN

0022-3670

Author

Cessi, Paola

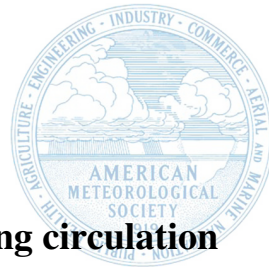
Publication Date

2020

DOI

10.1175/jpo-d-20-0026.1

Peer reviewed



Control of Bering Strait transport by the meridional overturning circulation

Paola Cessi*

Scripps Institution of Oceanography, University of California, San Diego, USA.

Downloaded from <http://journals.ametsoc.org/jpo/article-pdf/doi/10.1175/JPO-D-20-0026.1/4937480/jpo200026.pdf> by guest on 23 June 2020

*Corresponding author: Paola Cessi, pcessi@ucsd.edu, Scripps Institution of Oceanography,
University of California, San Diego,
La Jolla, CA 92039-0213, USA.

Early Online Release: This preliminary version has been accepted for publication in *Journal of the Physical Oceanography*, may be fully cited, and has been assigned DOI 10.1175/JPO-D-20-0026.1. The final typeset copyedited article will replace the EOR at the above DOI when it is published.

ABSTRACT

7 It is well-established that the mean transport through Bering Strait is balanced by a sea-level
8 difference between the North Pacific and the Arctic ocean, but no mechanism has been proposed to
9 explain this sea-level difference. It is argued that the sea-level difference across Bering Strait, which
10 geostrophically balances the northward throughflow, is associated with the sea-level difference
11 between the North Pacific and the North Atlantic/Arctic. In turn, the latter difference is caused
12 by deeper mid-depth isopycnals in the Indo-Pacific than in the Atlantic, especially in the northern
13 high-latitudes because there is deep water formation in the Atlantic, but not in the Pacific. Because
14 the depth of the mid-depth isopycnals is associated with the dynamics of the upper branch of the
15 meridional overturning circulation (MOC), a model is formulated which quantitatively relates the
16 sea-level difference between the North Pacific and the Arctic/North Atlantic with the wind-stress
17 in the Antarctic Circumpolar region, since this forcing powers the MOC, and with the outcropping
18 isopycnals shared between the northern hemisphere and the Antarctic circumpolar region, since
19 this controls the location of deep water formation. This implies that if the sinking associated with
20 the MOC were to occur in the North Pacific, rather than the North Atlantic, then the Bering Strait
21 flow would reverse. These predictions, formalized in a theoretical box model, are confirmed by
22 a series of numerical experiment in a simplified geometry of the world ocean, forced by steady
23 surface wind-stress, temperature and freshwater flux.

24 **1. Introduction**

25 Bering Strait connects the North Pacific and the Arctic oceans at about 66° N: with an average
26 depth of 50m and a minimum width of 85km, its climatologically averaged transport is northward
27 (from the Pacific into the Arctic) and about 0.8Sv (1 Sverdrup= $10^6\text{m}^3/\text{s}$) – increased to 1Sv for
28 the period 2003-2015 – with seasonal minimum in winter of 0.5Sv and maximum in summer of
29 1.5Sv (Woodgate 2018). The seasonal modulation of the transport is correlated with the local
30 wind, south-westward and strong in winter and weak in summer, which tends to drive the flow
31 towards the south. Occasionally the wind reverses the flow, and the transport becomes opposite to
32 the climatological direction.

33 The net northward flow is geostrophically balanced by a pressure and sea-surface height (SSH)
34 difference between the western and eastern sides of the strait (Toulany and Garrett 1984; Panteleev
35 et al. 2010; Woodgate 2018) of about 0.2m. This SSH difference is due to two processes: (1)
36 the along-strait wind-stress is frictionally balanced by an along strait velocity (southward), which
37 is in geostrophic balance with the across-strait SSH difference; (2) a large-scale pattern of SSH,
38 with the North Pacific standing higher than the Arctic and the North Atlantic. In the 21st century,
39 the locally wind-driven SSH difference produces an average transport of about -0.1Sv, while the
40 SSH difference between the North Pacific and the Arctic produces an average transport of about
41 1.1Sv (Woodgate 2018). Here the focus is on the latter process, which accounts for the sign and
42 magnitude of the climatological Bering Strait transport.

43 Detailed observations show that the Bering Strait transport associated with the SSH difference
44 between the North Pacific and the Arctic has little seasonal variation (Aagaard et al. 2006; Woodgate
45 2018), in contrast with the component associated with the local wind-stress. Given the large
46 seasonal cycle of the atmospheric conditions in this high-latitude region, the weak seasonality

47 suggests that this component of the SSH is not determined by local processes. Figure 1 shows
48 the climatological SSH anomalies from a comprehensive reanalysis of global observations (Forget
49 et al. 2015; Fukumori et al. 2017). Representative values are: in the high-latitude North Pacific at
50 60°N and 165°W , $\text{SSH}=0.19\text{m}$; in the high-latitude North Atlantic at 60°N and 5°E , $\text{SSH}=-0.43\text{m}$,
51 resulting in an SSH difference of about 0.6m . This difference is larger by a factor of three than
52 the typical difference between the South Pacific and South Atlantic basins. For example, at 30°S
53 and 72°W the SSH is 0.12m , while at 30°S and 16°E it is -0.12m . Thus, the SSH difference that
54 balances the climatological northward flow at Bering Strait has large-spatial and long-time scales
55 and is part of the global ocean circulation, rather than a regional phenomenon. It is noteworthy
56 that the variation in SSH along the eastern boundary of the Pacific is smaller than on the eastern
57 boundary of the Atlantic.

58 Indeed, regional models of the North Pacific – Arctic region require the prescription of SSH,
59 temperature and salinity and, in some cases, velocities at their outer open boundaries in order
60 to properly simulate the Bering transport (Zhang et al. 2010; Nguyen et al. 2011; Danielson
61 et al. 2011). Another regional model, with closed outer boundaries at 30°N , achieves a pressure
62 difference between the Atlantic and Pacific by blowing a 0.175N/m^2 westward wind-stress along
63 an artificial channel that crosses the North American continent from from coast to coast at 30°N
64 (Maslowski et al. 2004; Kinney et al. 2014). Other regional models that do not include remote
65 SSH differences or inflow-outflow at the outer boundaries can simulate the anomalies of Bering
66 Strait transport, but not its climatological mean: Danielson et al. (2014) shows that local wind
67 and sea-level pressure forcing and shelf waves dynamics account for about half of the transport
68 variability, but produce near-zero climatological Bering-Strait transport.

69 Perhaps counterintuitively, a comparison of four regional and one global model shows that the
70 climatological transport and temperature distribution at Bering Strait is represented better in a

71 model with only three grid-points across the strait than in models with higher resolution (Kinney
72 et al. 2014). Additionally, the state estimate provided at one-degree resolution by Estimating
73 the Circulation and Climate of the Ocean (version 4, release 3) (ECCO4 henceforth) has 1Sv
74 going through Bering Strait with a single grid point at the strait (the Bering Strait transport
75 *is not* a constraint assimilated in ECCO4) (Forget et al. 2015; Fukumori et al. 2017). These
76 modelling results provide additional evidence that the climatological transport is not controlled by
77 geographically local processes.

78 The body of observations and simulations summarized above clarify that the SSH difference
79 between the North Pacific and the Arctic/North Atlantic is essential to dynamically balance the
80 climatological transport through Bering Strait. Thus, in order to understand the control of the
81 time-mean Bering Strait throughflow, the time-mean SSH difference mentioned above must be
82 explained.

83 Almost sixty years ago Reid (1961) documented an observed difference in SSH between the
84 Pacific and Atlantic, relative to 1000db. A convincing dynamical theory for this difference was
85 provided only recently by Jones and Cessi (2016) and Thompson et al. (2016): the ageostrophic
86 transport entering the upper waters (above about 1000m) of the Indo-Pacific sector from the
87 Southern Ocean must exit this sector in the Southern Hemisphere and enter the Atlantic sector
88 where it eventually sinks to form North Atlantic Deep Water (NADW). This interbasin transport is
89 geostrophically balanced by a difference in pressure between the eastern boundaries of the South
90 Pacific and South Atlantic, which manifests itself as a difference in SSH and in isopycnal depths.
91 Numerical experiments show that when deep water formation moves from the North Atlantic to the
92 North Pacific (by manipulating the freshwater fluxes in the northern high latitudes of the basins),
93 the SSH and pressure difference between the Pacific and Atlantic changes sign, i.e. SSH is higher in
94 the Atlantic than in the Pacific (Hu et al. 2011; Jones and Cessi 2016; Cessi and Jones 2017). Thus,

95 the interbasin Pacific-Atlantic SSH difference is associated with the localization of the meridional
96 overturning circulation (MOC).

97 A series of numerical experiments where the Atlantic MOC (AMOC) is weakened by the addition
98 of freshwater in the Arctic (Hu and Meehl 2005; Hu et al. 2008, 2011) further shows that the location
99 of deep water formation controls the climatological Bering Strait transport (Hu and Meehl 2005;
100 Hu et al. 2008, 2011). The Bering Strait transport weakens with the AMOC, and even reverses
101 when the AMOC collapses. In the AMOC-collapsed state the Bering Strait transport is -1Sv, i.e.
102 equal and opposite to the value in the unperturbed, AMOC-on control case, and SSH is higher in
103 the Atlantic/Arctic relative to the Pacific (Hu et al. 2011).

104 Despite the evidence from observations and results from comprehensive ocean models showing
105 the global control of the SSH difference and flow through Bering Strait, no conceptual framework
106 has been put forward to explain the connection between the global overturning circulation, large-
107 scale SSH differences and the Bering Strait throughflow.

108 The only relevant study is De Boer and Nof (2004) who considered the momentum, volume,
109 temperature and salinity budgets of the Atlantic. The momentum budget uses “Godfrey’s island
110 rule” (Godfrey 1989) for the AMOC’s upper branch with the American continent as the “island”,
111 assuming that the pressure is constant all along the eastern boundaries of the Atlantic and Indo-
112 Pacific basins. This assumption is problematic for the Atlantic because in the sinking region
113 mixing is large and the pressure is no longer constant along the eastern boundary (Sumata and
114 Kubokawa 2001). Indeed, the outcropping of isopycnals associated with NADW production is a
115 central element to the theoretical framework for the climatological Bering Strait transport offered
116 here. In addition, De Boer and Nof (2004) neglect the baroclinic form-stress between the tips
117 of South Africa and South America associated with eddy transport and the diapycnal upwelling,
118 which are important contributors to the AMOC.

119 In the following we build a conceptual model that relates the SSH difference across Bering Strait,
120 and the associated transport, to the meridional overturning circulation. The predictions of the theory
121 are tested against numerical solutions of the primitive equations in a simplified configuration of
122 the world ocean. The goal of these simplified models is not to simulate the detailed features of the
123 circulation in the Bering Strait and its surrounding region, but rather to understand the important
124 process that maintains the climatological SSH difference and transport across Bering Strait against
125 the local wind-stress and friction, both of which tend to oppose the northward flow. Thus, we
126 quantify how the *sign and magnitude* of the SSH difference across the strait is related to the global
127 mid-depth overturning circulation. This is a complementary approach to that of the regional models
128 summarized in Kinney et al. (2014), which impose this SSH difference at the outer boundary of
129 the domain.

130 2. Conceptual model

131 The essential element of the theory is that the SSH difference across Bering Strait is dominated
132 by the large-scale difference in sea-level associated with outcropping of dense isopycnals in the
133 North Atlantic, but not in the North Pacific. This North-Atlantic outcropping marks the sinking
134 region of the MOC and the formation of NADW, and is absent in the Indo-Pacific.

135 The pressure difference across Bering Strait can be determined by assuming that the velocities
136 are geostrophically balanced, and thus pressure and SSH are constant all along the uninterrupted
137 portions of the Pacific northern boundary and the Arctic southern boundaries. In this way, the
138 pressure and SSH at the eastern (western) boundary of Bering Strait are given by the pressure and
139 SSH at the north east corner of the Pacific (Atlantic) basin. In turn, the pressure and SSH along the
140 eastern boundary of the Pacific basin (including the north-east corner) is geostrophically balanced,
141 and thus constant, and determined at the south-east corner of the Pacific basin.

142 The Pacific basin eastern boundary pressure is quantified using the buoyancy, mass and mo-
143 mentum budget of the upper limb of the MOC, which involves consideration of the global ocean,
144 including the Atlantic, Indo-Pacific and Southern Ocean sectors (Cessi 2019; Johnson et al. 2019).
145 In the spirit of Gnanadesikan (1999), Jones and Cessi (2016) and Cessi and Jones (2017), the
146 budget is performed above an isopycnal of depth h , i.e. the depth of the densest isopycnal that
147 outcrops on the eastern boundary of the North Atlantic, where NADW forms. The isopycnal of
148 depth h approximately separates the upper and lower limbs of the MOC, and it is called “separating
149 depth” henceforth: typical values for h are 1200m, much deeper than the depth of the subtropical
150 thermocline. A further simplification is to combine all the density classes above the separating
151 depth into an average value ρ_1 , and all the density classes below $z = -h$ into an average value ρ_0 .
152 With reference to figure 2, the sources and sinks of buoyancy above the separating isopycnal of
153 depth h are shown. The quantitative budget is expressed in terms of two unknowns, h_a and h_p ,
154 which are the constant values of h at the eastern boundary of the Atlantic-like basin (narrow) and
155 of the Pacific-like basin (wide), respectively. The important point is that h is constant and has
156 the value h_p all along the west coast of the American continent, i.e. the eastern boundary of the
157 Pacific-like basin, while h vanishes near the latitudes separating the North Atlantic and the Arctic,
158 i.e. near the north-east corner of the Atlantic Basin.

159 The buoyancy budget just described provides the pressure and SSH at the north-east bound-
160 aries of the North Atlantic and North Pacific. Assuming further that the pressure and SSH are
161 geostrophically balanced and thus constant along the northern boundary of the Pacific and the
162 southern boundary of the Arctic, the SSH and pressure can be determined at the eastern and
163 western sides of Bering Strait.

164 *a. Relating the SSH at Bering Strait to h*

165 The flow through Bering Strait is assumed to be in geostrophic balance, and thus proportional to
 166 $p_e - p_w$, where p_e and p_w are the pressures on the eastern and western sides of the strait respectively.
 167 Because of the shallowness of strait, the pressure difference $p_e - p_w$ can be considered independent
 168 of depth. The pressure can be calculated using the linear free surface approximation (Gill and
 169 Niller 1973)

$$p(x, y, z, t) = p_{atm}(x, y, t) + \rho_o g \eta(x, y, t) - \int_z^0 g \rho(x, y, z', t) dz', \quad (1)$$

170 where p_{atm} is the sea-level pressure (SLP), η is the SSH, g is the gravitational acceleration and ρ_o
 171 is the Boussinesq reference pressure. Evaluating (1) at $z = 0$, the height of the geoid, we obtain
 172 that the pressure difference across Bering Strait is given by

$$p_e - p_w = \Delta p_{atm} + \rho_o g \Delta \eta, \quad (2)$$

173 where

$$\Delta \eta \equiv \eta(x_E, 66^\circ \text{N}) - \eta(x_W, 66^\circ \text{N}) \quad (3)$$

174 is the SSH difference across Bering Strait and Δp_{atm} is the atmospheric pressure difference. The
 175 latter will be neglected henceforth, assuming that the climatological atmospheric pressure has a
 176 horizontal scale much larger than the strait width. Thus, the geostrophically balanced Bering Strait
 177 transport, T_{BS} , is given by

$$T_{BS} = H_{BS} \frac{g \Delta \eta}{f_{BS}}, \quad (4)$$

178 where H_{BS} is the depth of Bering Strait, considered constant, and f_{BS} is the Coriolis parameter at
 179 66°N .

180 We now assume that the pressures p_e and p_w at $z = 0$ are constant along uninterrupted solid
 181 boundaries because of geostrophy, so they can be calculated at the northern edge of the eastern

182 boundaries of the North Pacific and North Atlantic respectively. With reference to the lower panel
 183 of figure 2, we assume that the pressure and η are constant along the segment D-E and along the
 184 segment B-C, so that p_e is the pressure at $z = 0$ of point E (the north-east corner of the Pacific
 185 basin) and p_w is the pressure at $z = 0$ of point C (the north-east corner of the Atlantic basin).

186 In the basin regions, the SSH can be related to the depth h using the one-and-a-half layer
 187 approximation of (1)

$$g\eta(x,y,t) = -\frac{p_{atm}(x,y,t)}{\rho_o} + \frac{p_o}{\rho_o} + g\frac{\rho_o - \rho_1}{\rho_o}h(x,y,t), \quad (5)$$

188 where p_o is the constant pressure below $z = -h$.

189 Neglecting p_{atm} , the SSH difference across Bering Strait, $\Delta\eta$, is given by

$$g\Delta\eta \approx g'h_p, \quad (6)$$

190 where $g' \equiv g(\rho_o - \rho_1)/\rho_o$ is the range of surface buoyancies shared between the Antarctic circum-
 191 polar region and the region of deep water formation in the Northern Hemisphere (Wolfe and Cessi
 192 2010). Because there is no deep water formation in the Pacific, the geostrophic pressure and η
 193 are constant on the arclength comprising the eastern boundary of the Pacific basin and the eastern
 194 half of the northern boundary of the Pacific, so along this arclength $g\eta = p_o/\rho_o + g'h_p$. Similarly,
 195 because the interface outcrops at the northern edge of the eastern boundary of the North Atlantic,
 196 the SSH all along the western half of the northern solid boundary of the Pacific (on the Arctic
 197 side) is $g\eta = p_o/\rho_o$. Unlike the pressure and separating depth in the Pacific h cannot be considered
 198 constant all along the arclength of the eastern boundary of the Atlantic: in the deep water formation
 199 region mixing becomes important and at the north-east corner of the Atlantic basin $h = 0$, while it
 200 has a finite value $h = h_a$ along the eastern boundary away from the mixing region.

201 An implicit assumption of the theory is the neglect of friction and any along-coast wind-stress on
202 the boundary arclength, which would modify the pressure and thus the SSH along the boundaries'
203 arclengths.

204 It is now possible to directly relate the Bering Strait transport, T_{BS} , to h_p , through the geostrophic
205 relation

$$T_{BS} = H_{BS} \frac{g' h_p}{f_{BS}}. \quad (7)$$

206 The local wind-stress is neglected in (7), because we focus on the large-scale, rather than local,
207 SSH signal. Similarly, friction is neglected, even though it presumably has some influence in such
208 a narrow and shallow strait (Stigebrandt 1984).

209 With reference to figure 2, we can now evaluate h_p by considering the buoyancy budget of two
210 regions between $z = -h$ and the sea-surface: the global domain north of 52°S , and the Pacific-like
211 subdomain north of 30°S .

212 *b. The buoyancy budget above the separating depth h*

213 In the following we derive the details of the model. In summary, the MOC is powered by the
214 Ekman transport in the circumpolar region, taken at its maximum, i.e. at the subpolar/subtropical
215 boundary of the Southern Ocean. The steepening of the outcropping isopycnal due to the Ekman
216 cell in the circumpolar region is counteracted by eddy-fluxes of buoyancy (Gnanadesikan 1999;
217 Marshall and Radko 2003), parametrized as diffusion of isopycnal thickness, with constant eddy-
218 diffusivity κ_{GM} (Gent and McWilliams 1990; Griffies 1998): the slope of the isopycnal is then
219 approximated to be linear between the latitude of interest and the outcrop latitude in the southern
220 circumpolar region.

221 The goal of the conceptual model is to express the buoyancy budget in term of two unknowns,
222 i.e. the constant values of the separating depth at the eastern boundaries of the basins h_p and h_a ,

223 given the values of the external parameters that characterize the wind-stress, the surface buoyancy
 224 and the geometry of the domain. We derive two equations in the two unknowns h_p and h_a using
 225 the momentum, buoyancy, hydrostatic and continuity equations, following Gnanadesikan (1999)
 226 and Jones and Cessi (2016).

227 Although h vanishes in the sinking region, it has a finite depth elsewhere and the Atlantic-
 228 like (narrow) basin participates in the global buoyancy budget, primarily by hosting the sinking
 229 associated with the MOC. In the following, we denote with h_a the constant value of the isopycnal
 230 depth on the eastern side of the Atlantic-like basin away from the sinking region, and we use (6)
 231 for the evaluation of the geostrophically balanced Bering Strait transport.

232 The buoyancy budget can be obtained by integrating the continuity equation, $\nabla \cdot \mathbf{v} = 0$, above the
 233 separating depth $z = -h$ in the vertical and over the area of the domain of interest in the horizontal,
 234 i.e.

$$\int_A \mathrm{d}\mathbf{a} \int_{-h}^0 \nabla \cdot \mathbf{v} \, \mathrm{d}z = 0, \quad (8)$$

235 where $\mathbf{v} \equiv (u, v, w)$ is the three-dimensional velocity vector in depth coordinates and A is the
 236 horizontal area of the domain of interest. The integrated continuity equation can also be written as

$$\nabla \cdot \int_A \mathbf{u} h \, \mathrm{d}\mathbf{a} + \int_A (E - P - R + \eta_t + h_t - \varpi) \, \mathrm{d}\mathbf{a} = 0, \quad (9)$$

237 where \mathbf{u} is the vertically averaged horizontal velocity, $E - P - R$ is (minus) the net surface freshwater
 238 flux, ϖ is the diapycnal velocity across $z = -h$, and h_t and η_t are the tendency of h and η respectively.
 239 The tendency terms vanish when considering the climatological average, and the freshwater flux
 240 is neglected henceforth. Performing the integral over longitude on the first term of (9) in a domain
 241 either bounded by solid walls or periodic in longitude removes the dependence on the zonal
 242 component of the velocity leaving the following terms

$$L_x (\bar{v} \bar{h} + \overline{v' h'}) \Big|_{\text{South}}^{\text{North}} - \int_A \varpi \, \mathrm{d}\mathbf{a} = 0, \quad (10)$$

243 where \bar{v} and \bar{h} are the meridional velocity and separating depth respectively, zonally averaged over
 244 the longitudinal width L_x , and $\overline{v'h'}$ is the meridional transport of thickness associated with waves
 245 and eddies, zonally averaged over L_x . These quantities are evaluated at the southern and northern
 246 boundaries of the domain of interest.

247 With reference to the lower panel of figure 2, we first consider the domain bounded by $\theta_c = 52^\circ\text{S}$
 248 and $\theta = 66^\circ\text{N}$ in latitude and comprising all longitudes. Because of the circumpolar geometry at
 249 θ_c , there is no zonally averaged geostrophic meridional transport and $\bar{v}\bar{h}|_{\theta_c} = -\tau_c/(\rho_o f_c)$, i.e. the
 250 ageostrophic Ekman transport at 52°S . We parameterize the eddy thickness transport following
 251 Gent and McWilliams (1990), so that $\overline{v'h'} = -\kappa_{GM}\bar{h}_y$, with κ_{GM} constant. Assuming that the
 252 slope of the isopycnal is linear in the circumpolar region we get $\bar{h}_y|_{\theta_c} = \bar{h}|_{\theta_c}/L_c$, where L_c is the
 253 meridional distance between the Southern Hemisphere outcrop and θ_c . We then identify $\bar{h}|_{\theta_c}$ with
 254 h_p .

255 There are two terms associated with the area-integrated diapycnal velocity at the separating depth
 256 $z = -h$: the diffuse upwelling due to diapycnal mixing and the sinking due to NADW formation.
 257 To estimate the mixing term, we use scale analysis, while the sinking term is equal to (the negative
 258 of) the zonal integral of the geostrophically balanced meridional transport in the upper branch of
 259 the AMOC just south of the outcrop. Thus, we have

$$\int_A \overline{\omega} \, da = \underbrace{\frac{\kappa A_a}{h_a} + \frac{\kappa A_p}{h_p}}_{\text{Diffusive}} - \underbrace{g' \frac{h_a^2 - h_w^2}{2f_{BS}}}_{\text{Sinking}}, \quad (11)$$

260 where κ is the diapycnal diffusivity, A_a, A_p are the areas of the Atlantic and Indo-Pacific sectors
 261 respectively, and h_w is the depth of the isopycnal interface on the western boundary of the North
 262 Atlantic sector just south of the outcrop. In this subpolar region h_w is much smaller than h_a , and
 263 can be neglected. In other words, sinking is assumed to occur at a lower latitude on the western
 264 boundary relative to the eastern boundary.

265 In summary, the global buoyancy budget in the region between 52°S and 66°N and above the
 266 separating depth can be expressed as

$$\underbrace{\frac{\tau_c L}{\rho_o f_c}}_{\text{Ekman}} - \underbrace{\frac{\kappa_{GM} h_p L}{L_c}}_{\text{Eddy}} + \underbrace{\frac{\kappa A_a}{h_a} + \frac{\kappa A_p}{h_p}}_{\text{Diffusive}} = \underbrace{g' \frac{h_a^2}{2 f_{BS}}}_{\text{Sinking}} \quad (12)$$

267 A second relation is obtained considering the buoyancy budget above the separating depth in the
 268 Indo-Pacific sector between 30°S and 66°N. In addition to terms analogous to those entering the
 269 global budget, we must also consider a geostrophically balanced interbasin meridional transport
 270 at 30°S, given by $g'(h_p^2 - h_a^2)/(2f_s)$, as well as the transport through Bering Strait, both exchanged
 271 between the Atlantic and the Indo-Pacific basins. The budget in the Indo-Pacific gives:

$$\underbrace{\frac{\tau_s L_p}{\rho_o f_s}}_{\text{Ekman}} - \underbrace{\frac{\kappa_{GM} h_p L_p}{L_s}}_{\text{Eddy}} + \underbrace{\frac{\kappa A_p}{h_p}}_{\text{Diffusive}} + \underbrace{\frac{g'(h_p^2 - h_a^2)}{2 f_s}}_{\text{Interbasin}} = \underbrace{H_{BS} \frac{g' h_p}{f_{BS}}}_{T_{BS}} \quad (13)$$

272 where the definition and typical values of the symbols used in (12-13) are given in table 1.

273 There are several differences between our approach and that of De Boer and Nof (2004): in our
 274 approach the SSH on the western side of Bering Strait takes into account the outcropping of the
 275 mid-depth isopycnals in the North Atlantic associated with NADW formation, while the treatment
 276 of the SSH on the eastern side of the strait coincides in the two theories; we include the transport of
 277 buoyancy by eddies in the Southern Ocean, appropriately parameterized, and the diapycnal mixing
 278 at the interface depth, while these effects are neglected in De Boer and Nof (2004); we give explicit
 279 expressions for the different terms contributing to the buoyancy budget in terms of the eastern
 280 boundary pressures, h_a and h_p , using the approximate momentum balance.

281 The algebraic coupled system (12-13) is easily solved numerically for h_a and h_p , but it is is
 282 useful to calculate an approximate solution valid for wind-stress in the range of the Southern Ocean

283 westerlies, i.e.

$$h_a \approx \sqrt{-\frac{2f_{BS}\tau_c L}{g'\rho_o f_c}}, \quad h_p \approx \sqrt{-\frac{2f_{BS}\tau_c L}{g'\rho_o f_c} + \frac{2\tau_s L_p}{g'\rho_o}}. \quad (14)$$

284 Figure 4 shows the dependence of h_a and h_p as a function of the amplitude of the wind stress,
285 measured by the maximum westerly wind-stress in the Southern Ocean, for the parameter values
286 given in table 1. The important points are: (1) the depth of the isopycnal bounding the upper limb
287 of the MOC from below increases as the square root of the wind-stress in the Southern Ocean
288 (Gnanadesikan 1999), except for small values of the wind-stress, in which case the eddy transport
289 and diapycnal terms become important; (2) $h_p > h_a$ so that the interbasin exchange, proportional
290 to $(h_p^2 - h_a^2)/f_s$, is negative (recall that $f_s < 0$), i.e. from the Pacific-like basin into the Atlantic-like
291 basin (Jones and Cessi 2016; Cessi and Jones 2017). As advertised, the mid-depth isopycnals are
292 deeper in the Pacific than Atlantic and the SSH is higher in the Pacific than Atlantic, as observed
293 by Reid (1961).

294 The corresponding values for the Bering Strait transport, T_{BS} , as a function of the amplitude
295 of the wind stress are shown in figure 5, for the parameter values given in table 1. For the
296 oceanographically relevant range of $\tau_c = 0.1 - 0.2$ Pa the geostrophically balanced Bering Strait
297 transport is 2.5-3.2 Sv, i.e. about two-three times larger than observations. As shown in section
298 3 these predictions are correct given the geometry of the domain, which neglects the Arctic shelf,
299 and the wind-stress at the latitude of Bering Strait.

300 Another prediction of the model is that the flow through Bering Strait should reverse if sinking
301 were to occur in the Pacific-like basin. Figure 3 shows the geometry of the isopycnal separating
302 the upper and lower limb of the overturning in this case: the isopycnal vanishes at the latitude of
303 Bering Strait on the Pacific (east) side ($h_p = 0$ at the latitude of Bering Strait), rather than on the

304 Atlantic (west) side. Thus the Bering Strait transport is now given by

$$T_{BS} = -H_{BS} \frac{g' h_a}{f_{BS}}, \quad (15)$$

305 and the transport is negative (southward). The depth of the isopycnal, measured by h_a and h_p is
 306 now governed by

$$\underbrace{-\frac{\tau_c L}{\rho_o f_c}}_{\text{Ekman}} \underbrace{-\frac{\kappa_{GM} h_p L}{L_c}}_{\text{Eddy}} + \underbrace{\frac{\kappa A_a}{h_a} + \frac{\kappa A_p}{h_p}}_{\text{Diffusive}} = \underbrace{g' \frac{h_p^2}{2 f_{BS}}}_{\text{Sinking}}, \quad (16)$$

307 and

$$\underbrace{-\frac{\tau_s L_p}{\rho_o f_s} + \frac{\tau_c L}{\rho_o f_c}}_{\text{Ekman}} \underbrace{-\frac{\kappa_{GM} h_p L_p}{L_s} + \frac{\kappa_{GM} h_p L}{L_c}}_{\text{Eddy}} \underbrace{-\frac{\kappa A_a}{h_a}}_{\text{Diffusive}} + \underbrace{\frac{g'(h_p^2 - h_a^2)}{2 f_s}}_{\text{Interbasin}} = \underbrace{-H_{BS} \frac{g' h_a}{f_{BS}}}_{T_{BS}}. \quad (17)$$

308 In this case the approximate solution of (16-17), valid for oceanographically relevant wind -stress
 309 is

$$h_p \approx \sqrt{-\frac{2 f_{BS} \tau_c L}{g' \rho_o f_c}}, \quad h_a \approx \sqrt{-\frac{2 \tau_c L}{g' \rho_o f_c} (f_{BS} - f_s) - \frac{2 \tau_s L_p}{g' \rho_o}}. \quad (18)$$

310 As before, the numerical solution of (16) and (17) agrees with the approximation (18) (figure
 311 not shown). The important point is that, to a first approximation, the Bering Strait transport is
 312 proportional to the square root of the wind-stress in the Southern Hemisphere. This dependence
 313 is mediated by the depth of isopycnal separating the upper and lower limbs of the MOC in the
 314 non-sinking basin, which is directly proportional to the SSH difference between the North Pacific
 315 and the Atlantic at the latitudes of Bering Strait.

316 In the following, the predictions of the conceptual model are tested against solutions of the
 317 primitive equations in a simple geometrical configuration of the world ocean, forced by simplified
 318 wind-stress, temperature and freshwater fluxes, all prescribed at the surface.

319 **3. Results of a general circulation model**

320 The predictions and assumptions of the conceptual model are tested in an ocean general circulation
321 model (GCM), configured in an idealized global ocean geometry, as illustrated in figure 6. The
322 model is the MITgcm (Marshall et al. 1997) which solves the discretized primitive equations in a
323 spherical sector 210°-wide with solid boundaries to the south at 70°S and to the north at 80°N.
324 The domain is divided into semienclosed sub-basins separated by boundaries along the meridians
325 at 0° and 70°E. The narrow, Atlantic-like subbasin is 70° wide and has solid boundaries extending
326 from 52°S to 66°N at 0°E, representing the American (long) continent, and 30°S to 66°N at 70°E,
327 representing the Eurafrikan (short) continent. Both basins are open on the south to a region 210°-
328 periodic in longitude, which represents the Antarctic circumpolar region. In addition, the narrow
329 basin opens on the north to a region 210°-periodic in longitude representing the Arctic Ocean. The
330 wide, Pacific-like subbasin is closed to the north at 66°N, except for a Bering-like strait which is
331 67m deep and whose width is varied among solutions between 0 (closed strait), 136 (single strait),
332 272 (double strait) and 408km (triple strait). The model narrowest strait is almost twice as wide as
333 Bering Strait, and is resolved by three grid points in longitude, the minimum needed to calculate
334 the gradients of tracers and velocity.

335 Elsewhere, the domain is 4000m deep, except that south of the long continent there is a ridge
336 2000m high and 1°-wide in longitude. The model's resolution is 1° in latitude and longitude. In
337 the vertical direction there are 32 unequally-spaced levels with depths ranging from 6.8m near the
338 surface to 143m at the bottom. The equation of state is taken to be linear with thermal and ha-
339 line expansion coefficients equal to $2 \times 10^{-4} K^{-1}$ and $7.4 \times 10^{-4} PSU^{-1}$ respectively. Because the
340 resolution is insufficient to permit the development of baroclinic eddies, their effect on tracer trans-
341 port is parametrized using the GentMcWilliams advective parametrization (Gent and McWilliams

1990; Griffies 1998; Ferrari et al. 2010), and the isopycnal tracer mixing scheme described by Redi (1982), with equal constant coefficients of eddy diffusivity $\kappa_{GM} = \kappa_{Redi} = 500\text{m}^2/\text{s}$. The vertical diffusivity is set to $2 \times 10^{-5} \text{m}^2\text{s}^{-1}$ in the interior, increasing to $1 \times 10^{-2} \text{m}^2\text{s}^{-1}$ at the surface over a depth of 30m to model the mixed layer. A simple convective adjustment scheme is used where vertical tracer diffusivity is increased to $10\text{m}^2\text{s}^{-1}$ when stratification is statically unstable. Most ocean general circulation models, in addition to a surface mixed layer and a convective adjustment scheme use a diffusivity that increases with depth below 2500m (Bryan and Lewis 1979; Nikurashin and Ferrari 2013). The bottom-enhanced diapycnal diffusivity is well below the upper branch of the MOC, and while essential for the abyssal circulation, it is subdominant for the mid-depth circulation (Cessi 2019; Johnson et al. 2019), and is omitted here.

The surface forcing is prescribed as steady zonally uniform wind-stress (top panel of figure 7), relaxation to a zonally uniform temperature, T^* , with a time scale of 15 days (middle panel of figure 7), and freshwater flux (virtual salt flux) which is zonally uniform within each sector from 0°E to 70°E and from 70°E to 210°E , but varies between the two sectors in the latitudinal range from 25°N to 66°N , controlling the location of sinking (bottom panel of figure 7).

The model is integrated until statistical steady state is achieved, i.e. about 3000 years, starting from initial conditions in a nearby part of parameter space.

a. Varying the surface forcing

One of the main assumptions of the conceptual model is that the depth of the isopycnal separating the northward and southward limbs of the MOC is constant along each eastern boundary, while outcropping in the sinking sector at the latitude of Bering Strait. The conceptual model predicts that the depth of the isopycnal increases as the circumpolar wind-stress increases, and that it is shallower in the sinking basin. The assumptions and predictions are qualitatively confirmed by the

numerical simulations in line with previous work without a Bering-like strait (Gnanadesikan 1999; Jones and Cessi 2016; Cessi and Jones 2017). Figure 8 shows the density on the eastern boundary of the narrow basin (Atlantic-like) as a function of latitude and depth for the three wind-stress profiles shown in the top panel of figure 7, while using the freshwater flux profiles with the black lines in the bottom panel of figure 7. In the bottom right panel of figure 8 the freshwater flux is changed to the profiles with the blue lines in the bottom panel of figure 7, inducing sinking in the Pacific-like (wide) basin (bottom right panel). The corresponding densities on the eastern boundary of the Pacific-like (wide) basin are shown in figure 9. The main point is that above the separating depth of the MOC (i.e. above the isopycnal marked by a thick line) are systematically shallower in the sinking basin, outcropping before or at the latitude of the strait (marked by a white line, bold in the wide basin and dashed in the narrow basin).

The corresponding overturnings are visualized using the zonally and time-averaged residual streamfunction, ψ , defined as

$$\psi(y, \tilde{\rho}) \equiv -\frac{1}{TL} \int_0^T dt \int_0^L dx \int_{-H}^0 v^\dagger(x, y, z, t) \mathcal{H}[\rho(x, y, z, t) - \tilde{\rho}] dz. \quad (19)$$

where $T = 100$ years, $v^\dagger = v + v_{GM}$ is the total meridional velocity (the sum of the resolved velocity, v , and the eddy velocity from the GM parameterization, v_{GM}), and \mathcal{H} is the Heaviside step function. ψ is the zonally integrated transport of water below the isopycnal $\rho(x, y, z, t) = \tilde{\rho}$. The “vertical” coordinate $\tilde{\rho}$ is density; the tilde distinguishes the label of a density surface from the density field (Young 2012). The domain for the zonal integration, L , can be either the narrow sector (0°E to 70°E) or the wide sector (140°W to 0°E) between the latitudes occupied by the short continent (30°S to 66°N), but includes the whole zonal extent elsewhere (i.e. for latitudes north of 66°N or south of 30°S).

386 For presentation purposes, ψ is remapped into height coordinates using the mean isopycnal height

$$\zeta(y, \bar{\rho}) \equiv -\frac{1}{TL} \int_0^T dt \int_0^L dx \int_{-H}^0 \mathcal{H}[\rho(x, y, z, t) - \bar{\rho}] dz. \quad (20)$$

387 The residual overturning streamfunction for the forcings corresponding to the density fields in
388 figures 8 and 9 is shown in figures 10 and 11. The important points are: (1) the interhemispheric
389 overturning strength increases with the wind-stress in the circumpolar region (Toggweiler and
390 Samuels 1993, 1995; Gnanadesikan 1999; Nikurashin and Vallis 2012); (2) the interhemispheric
391 overturning is accompanied by an interbasin exchange in the non-sinking basin which is expressed
392 as a southward flow at intermediate depths, and a deeper northward return flow (Ferrari et al. 2017).

393 The strait transport reverses when the sinking is localized in the wide basin, with a magnitude
394 almost equal and opposite to the case of narrow-basin sinking. The reversal in transport is
395 accompanied by a reversal in the sea surface height gradient across the strait and between the
396 subpolar region of the subbasins, as shown in figure 6. This behavior is consistent with that found
397 in more comprehensive climate models (Hu and Meehl 2005; Hu et al. 2008, 2011).

398 Notice that when the overturning is localized in the narrow basin, sinking occurs both in the
399 basin and in the Arctic-like portion of the domain, where densities are highest, while sinking in the
400 wide basin (bottom left corners of figures 10 and 11) occurs south of the strait at lower densities.
401 With the linear equation of state and constant ocean depth, when sinking is in the narrow basin,
402 the densest water at surface is in the Northern Hemisphere, and abyssal water is formed there.
403 In contrast, when sinking occurs in the wide basin, the densest surface water is in the Southern
404 Hemisphere, and abyssal water is formed there. In the latter case, an abyssal counterclockwise
405 cell exists, which pushes the MOC further up in the water column, as documented in Jansen and
406 Nadeau (2016). Remarkably, the details of the abyssal cell are irrelevant for Bering Strait transport,
407 whose magnitude is around 3Sv in all cases.

408 The increase in overturning is accompanied by an increase in $\Delta\eta$ at the strait, dominated by a large
409 decrease in the SSH on the western and northern side of the strait, i.e. the side determined by the
410 Atlantic dynamics. Figure 12 shows the SSH as a function of arclength along paths following the
411 eastern boundaries of both basins and the northern boundary of the wide basin (moving clockwise
412 for the narrow basin and counterclockwise for the wide basin). For reference, some landmark points
413 along the boundary path are shown in figures 12 and 2 (bottom panel). To guarantee continuity of
414 the pressure and SSH, the points on the northern boundary of the narrow basin are evaluated one
415 grid-point *north* of the strait's latitude (dashed lines in figure 12, corresponding to the red line in
416 figure 2), while the points on the northern boundary of the wide basin are evaluated one grid-point
417 *south* of the solid boundary (solid lines in figure 12, corresponding to the blue line in figure 2).

418 The difference in SSH at the eastern boundaries is almost constant between 30°S and 55°N but
419 increases rapidly as deep isopycnals outcrop in the narrow basin, but not in the wide one. Indeed
420 the isopycnal bounding the upper branch of the MOC from below (thick black contour in figures 8
421 and 9) outcrops at the latitude of Bering Strait in the sinking basin but not in the non-sinking basin
422 (the white line in figures 8 and 9 marks the Bering Strait latitude).

423 The transport across the strait increases with the amplitude of the Southern Hemisphere winds,
424 as shown in figure 5, although not as fast as the inviscid model of section 2 predicts. In addition,
425 there is a dependence on the strait width which is not accounted for in the box model.

426 *b. Varying the strait width*

427 The conceptual model assumes that the transport and the SSH difference across the strait are
428 in geostrophic balance, independent of the strait width. This assumes that frictional effects are
429 negligible, as appropriate for a strait much larger (and deeper) than a frictional boundary layer width
430 (and depth). This assumption is contrary to a previous theoretical estimate of the Bering Strait

431 flow (Stigebrandt 1984), but it is confirmed by theoretical, numerical and observational estimates
432 (Toulany and Garrett 1984; Panteleev et al. 2010; Woodgate 2018). In the low-resolution, primitive
433 equation computations, we find that T_{BS} increases slightly with the strait width, indicating that the
434 geostrophic estimate is an upper bound for a strait with the actual size of Bering Strait, and that
435 in our model configuration friction becomes important for openings less than 136km (which is the
436 narrowest considered in our computations). It is possible that a higher resolution model would not
437 display the same sensitivity as the low-resolution computations.

438 Other geometrical aspects of the strait, neglected in the simplified model, might contribute to,
439 and mostly decrease, the transport: frictional effects in the shallow shelf on both sides of the strait
440 can break the geostrophic constraint along the coast, effectively decreasing the SSH signal along the
441 northern boundary of the Pacific and the southern boundary of the Arctic. In addition, the pressure
442 and SSH signal can be locally modified by along-strait wind-stress in combination with frictional
443 effects on the shallow shelf, by setting up a local sea-surface slope across the strait: this is the
444 process that induces a reduced or even reversed transport in the winter months (Woodgate 2018),
445 when there is a strong northerly wind. Finally, there is classical Ekman transport: a net westerly
446 wind-stress along the southern boundary of the Arctic would reduce the east-west difference in
447 SSH over the value obtained neglecting the coastal Ekman transport. In summary, it appears that
448 the local effects neglected here, i.e. shallow shelf, friction and local wind, tend to drive a southward
449 flow against the northward Bering Strait transport balanced by the large-scale pressure difference
450 between the North Atlantic and North Pacific.

451 **4. Summary and discussion**

452 We attribute the SSH difference across Bering Strait, which geostrophically balances the associ-
453 ated northward climatological transport, to the large scale difference in isopycnal depth associated

454 with the MOC. In particular, we focus on the isopycnals that separate the upper and lower limbs of
455 the MOC: these are the isopycnals that outcrop in the North Atlantic and Arctic, and are associated
456 with the formation of North Atlantic Deep Water. The same isopycnals do not outcrop in the North
457 Pacific and this leads to a large-scale difference in isopycnal depths in the northern latitudes of
458 these basins, resulting in a pressure and SSH difference across Bering Strait. The idea that the
459 MOC controls the Bering Strait throughflow has been proposed previously by De Boer and Nof
460 (2004), but not in terms of the relation between the SSH and the isopycnal difference between the
461 North Atlantic/Arctic and the North Pacific.

462 This hypothesis is quantified with both a one-and-a-half-layer box model, and a three-
463 dimensional, continuously stratified, primitive equations general circulation model, both in a sim-
464 plified geometry of the world ocean. It is remarkable how well the predictions of the one-and-a-
465 half-layer box model agree with those of the MITgcm, contingent on the choice of one parameter,
466 g' , which quantifies the range of outcropping buoyancies shared by the Antarctic circumpolar
467 region and the northern-hemisphere deep water formation region (Wolfe and Cessi 2010). In the
468 three-dimensional computations g' is determined by the dynamics of the MOC itself, given the
469 prescription of surface wind-stress, surface temperature and surface freshwater flux: because the
470 surface salt flux is prescribed, rather than the surface salinity, the surface buoyancies shared by
471 the sinking region and the Southern Ocean are part of the global solution. Yet, there is quantitative
472 agreement between the one-and-a-half-layer box model and the three-dimensional computations.

473 Unlike the computations of De Boer and Nof (2004), our model Pacific and Atlantic are connected
474 at high latitudes by circumpolar regions, periodic in longitude rather than bounded by meridional
475 barriers. This is an important detail, especially for the southern hemisphere connection, because
476 it is only in a circumpolar geometry that the surface Ekman transport is returned below the
477 bottom topography: in a domain bounded to the East and West the return of the Ekman transport

478 occurs within shallow wind-driven gyres, and there is no mid-depth stratification and overturning
479 circulation (Wolfe and Cessi 2010).

480 We show that the Ekman transport in the circumpolar region of the southern hemisphere controls
481 the SSH drop across Bering Strait, mediated by the MOC, and we quantify the dependence of the
482 climatological Bering Strait transport on the circumpolar wind-stress. The simplified geometry and
483 forcing overestimates the Bering Strait transport: we do not consider the effect of the shallow shelf
484 that surrounds Bering Strait and the associated bottom friction, which would limit the conservation
485 of pressure and SSH along the solid boundaries connecting to the strait, thus reducing the SSH
486 difference across the strait. According to the observations presented in figure 1, while the SSH
487 difference between the eastern boundaries of the high-latitude North Atlantic and of the high
488 latitude North Pacific is about 0.6m, the SSH difference drops to about 0.2m across Bering Strait.
489 Almost all of this drop occurs in the Arctic indicating that a substantial attenuation of the SSH
490 signal occurs on the Arctic shelf. In our shelf-less model the jump in SSH that occurs across the
491 strait between the Pacific-like region and the Atlantic/Arctic-like region is constant throughout the
492 Arctic's boundary, ranging from 0.6m to 0.8m depending on the strength of the ACC winds (cf. the
493 SSH difference between the points E and B in figure 12). Presumably, as in nature, this difference
494 would be decreased as Bering Strait is approached if a shelf were included.

495 We also ignore the coastal Ekman transport associated with wind-stress anywhere along the
496 southern boundary of the Arctic and along the eastern boundary of the Pacific: this wind-stress
497 would alter the SSH difference across Bering Strait. Finally, the local wind-stress at Bering Strait
498 is neglected: as detailed in Woodgate (2018) the along strait wind induces a transport parallel to
499 the wind, and thus southward in the prevailing northerlies of this region.

500 When the prescribed surface freshwater flux is contrived to induce deep water formation in the
501 North Pacific, rather than in the North Atlantic/Arctic, then the difference in SSH across Bering

502 Strait, and the associated transport are reversed. This result is consistent with previously published
503 numerical simulations in a realistic configuration of the world ocean (Hu and Meehl 2005; Hu
504 et al. 2008, 2011). As in those computations, we find that the sign of the transport is reversed,
505 but the amplitude is the same, consistently with the notion that the strength of the MOC and
506 the mid-depth stratification is controlled by the wind-stress and eddy transport in the Antarctic
507 circumpolar region and by the global diapycnal mixing, regardless of the sinking location. These
508 same processes control the SSH difference between the North Pacific and North Atlantic, and
509 ultimately the climatological sign and amplitude of Bering Strait transport.

510 *Acknowledgments.* Support by the National Science Foundation under Grant OCE-1634128 is
511 gratefully acknowledged. Computational resources were provided by the Extreme Science and
512 Engineering Discovery Environment (XSEDE) on Stampede2 at the Texas Advanced Comput-
513 ing Center through allocation TG-OCE130026. XSEDE is supported by the National Science
514 Foundation grant number ACI-1548562.

515 **References**

- 516 Aagaard, K., T. J. Weingartner, S. L. Danielson, R. A. Woodgate, G. C. Johnson, and T. E.
517 Whitley, 2006: Some controls on flow and salinity in Bering Strait. *Geophys. Res. Lett.*, **33**,
518 doi:10.1029/2006GL026612.
- 519 Bryan, K., and L. Lewis, 1979: A water mass model of the world ocean. *J. Geophys. Res.*, **84 (C5)**,
520 2503–2517.
- 521 Cessi, P., 2019: The Global Overturning Circulation. *Ann. Rev. Marine Science*, **11**, 249–270.
- 522 Cessi, P., and C. Jones, 2017: Warm-route versus cold-route interbasin exchange in the meridional
523 overturning circulation. *J. Phys. Oceanogr.*, **47**, 1981–1997.

- 524 Danielson, S., E. Curchitser, K. Hedstrom, T. Weingartner, and P. Stabeno, 2011: On ocean and
525 sea ice modes of variability in the Bering Sea. *J. Geophys. Res.*, **116** (C12).
- 526 Danielson, S. L., T. J. Weingartner, K. S. Hedstrom, K. Aagaard, R. Woodgate, E. Curchitser, and
527 P. J. Stabeno, 2014: Coupled wind-forced controls of the Bering–Chukchi shelf circulation and
528 the Bering Strait throughflow: Ekman transport, continental shelf waves, and variations of the
529 Pacific–Arctic sea surface height gradient. *Prog. Oceanogr.*, **125**, 40–61.
- 530 De Boer, A. M., and D. Nof, 2004: The Bering Strait’s grip on the northern hemisphere climate.
531 *Deep Sea Res. Part I: Oceanographic Research*, **51**, 1347–1366, doi:10.1016/j.dsr.2004.05.003.
- 532 Ferrari, R., S. M. Griffies, A. J. G. Nurser, and G. K. Vallis, 2010: A boundary-value problem
533 for the parameterized mesoscale eddy transport. *Ocean Modell.*, **32**, 143–156, doi:10.1016/j.
534 ocemod.2010.01.004.
- 535 Ferrari, R., L.-P. Nadeau, D. P. Marshall, L. C. Allison, and H. L. Johnson, 2017: A model of the
536 ocean overturning circulation with two closed basins and a reentrant channel. *J. Phys. Oceanogr.*,
537 **47**, 2887–2906.
- 538 Forget, G., J.-M. Campin, P. Heimbach, C. N. Hill, R. M. Ponte, and C. Wunsch, 2015: ECCO
539 version 4: an integrated framework for non-linear inverse modeling and global ocean state esti-
540 mation. *Geoscientific Model Development*, **8** (10), 3071–3104, doi:10.5194/gmd-8-3071-2015,
541 URL <http://www.geosci-model-dev.net/8/3071/2015/>.
- 542 Fukumori, I., O. Wang, I. Fenty, G. Forget, P. Heimbach, and R. M. Ponte, 2017: Ecco version 4
543 release 3. Tech. rep. doi:1721.1/110380, URL <http://hdl.handle.net/1721.1/110380>, available at
544 ftp://ecco.jpl.nasa.gov/Version4/Release3/doc/v4r3_estimation_synopsis.pdf.

- 545 Gent, P., and J. C. McWilliams, 1990: Isopycnal mixing in ocean circulation models. *J. Phys.*
546 *Oceanogr.*, **20**, 150–155, doi:10.1175/1520-0485(1990)020<0150:IMIOCM>2.0.CO;2.
- 547 Gill, A., and P. Niller, 1973: The theory of the seasonal variability in the ocean. *Deep Sea Research*
548 *and Oceanographic Abstracts*, Vol. 20, 141–177.
- 549 Gnanadesikan, A., 1999: A simple predictive model for the structure of the oceanic pycnocline.
550 *Science*, **283**, 2077–2079, doi:10.1126/science.283.5410.2077.
- 551 Godfrey, J., 1989: A sverdrup model of the depth-integrated flow for the world ocean allowing for
552 island circulations. *Geophysical & Astrophysical Fluid Dynamics*, **45 (1-2)**, 89–112.
- 553 Griffies, S. M., 1998: The Gent-McWilliams skew flux. *J. Phys. Oceanogr.*, **28 (5)**, 831–841.
- 554 Hu, A., and G. A. Meehl, 2005: Bering Strait throughflow and the thermohaline circulation.
555 *Geophys. Res. Lett.*, **32**, doi:10.1029/2005GL024424.
- 556 Hu, A., G. A. Meehl, W. Han, and J. Yin, 2011: Effect of the potential melting of the Greenland
557 Ice Sheet on the meridional overturning circulation and global climate in the future. *Deep Sea*
558 *Research Part II: Topical Studies in Oceanography*, **58**, 1914–1926.
- 559 Hu, A., B. L. Otto-Bliesner, G. A. Meehl, W. Han, C. Morrill, E. C. Brady, and B. Briegleb,
560 2008: Response of thermohaline circulation to freshwater forcing under present-day and LGM
561 conditions. *J. Climate*, **21**, 2239–2258.
- 562 Jansen, M. F., and L.-P. Nadeau, 2016: The effect of Southern Ocean surface buoyancy loss on the
563 deep-ocean circulation and stratification. *J. Phys. Oceanogr.*, **46**, 3455–3470.
- 564 Johnson, H. L., P. Cessi, D. P. Marshall, F. Schloesser, and M. A. Spall, 2019: Recent contributions
565 of theory to our understanding of the Atlantic Meridional Overturning Circulation. *J. Geophys.*
566 *Res.*, **124 (8)**, 5376–5399.

- 567 Jones, C. S., and P. Cessi, 2016: Interbasin transport of the meridional overturning circulation. *J.*
568 *Phys. Oceanogr.*, **46**, 1157–1169.
- 569 Kinney, J. C., and Coauthors, 2014: On the flow through Bering Strait: A synthesis of model
570 results and observations. *The Pacific Arctic Region*, Springer, 167–198.
- 571 Marshall, J., C. Hill, L. Perelman, and A. Adcroft, 1997: Hydrostatic, quasi-hydrostatic, and non-
572 hydrostatic ocean modeling. *J. Geophys. Res.*, **102 (C3)**, 5733–5752, doi:10.1029/96JC02776.
- 573 Marshall, J., and T. Radko, 2003: Residual-mean solutions for the Antarctic Circumpolar Current
574 and its associated overturning circulation. *J. Phys. Oceanogr.*, **33 (11)**, 2341–2354.
- 575 Maslowski, W., D. Marble, W. Walczowski, U. Schauer, J. L. Clement, and A. J. Semtner, 2004:
576 On climatological mass, heat, and salt transports through the Barents Sea and Fram Strait from
577 a pan-Arctic coupled ice-ocean model simulation. *J. Geophys. Res.*, **109 (C3)**.
- 578 Nguyen, A. T., D. Menemenlis, and R. Kwok, 2011: Arctic ice-ocean simulation with optimized
579 model parameters: Approach and assessment. *J. Geophys. Res.*, **116 (C4)**.
- 580 Nikurashin, M., and R. Ferrari, 2013: Overturning circulation driven by breaking internal waves
581 in the deep ocean. *Geophys. Res. Lett.*, **40**, 3133–3137.
- 582 Nikurashin, M., and G. Vallis, 2012: A theory of the interhemispheric meridional overturning
583 circulation and associated stratification. *J. Phys. Oceanogr.*, **42 (10)**, 1652–1667, doi:10.1175/
584 JPO-D-11-0189.1.
- 585 Panteleev, G., D. A. Nechaev, A. Proshutinsky, R. Woodgate, and J. Zhang, 2010: Reconstruction
586 and analysis of the Chukchi Sea circulation in 1990–1991. *J. Geophys. Res.*, **115 (C8)**.
- 587 Redi, M. H., 1982: Oceanic isopycnal mixing by coordinate rotation. *J. Phys. Oceanogr.*, **12**,
588 1154–1158, doi:10.1175/1520-0485(1982)012<1154:OIMBCR>2.0.CO;2.

- 589 Reid, J. L., 1961: On the temperature, salinity, and density differences between the atlantic
590 and pacific oceans in the upper kilometre. *Deep Sea Research*, **7 (4)**, 265 – 275, doi:doi:
591 10.1016/0146-6313(61)90044-2.
- 592 Stigebrandt, A., 1984: The North Pacific: a global-scale estuary. *J. Phys. Oceanogr.*, **14**, 464–470.
- 593 Sumata, H., and A. Kubokawa, 2001: Numerical study of eastern boundary ventilation and its
594 effects on the thermocline structure. *J. Phys. Oceanogr.*, **31 (10)**, 3002–3019.
- 595 Thompson, A. F., A. L. Stewart, and T. Bischoff, 2016: A multibasin residual-mean model for the
596 global overturning circulation. *J. Phys. Oceanogr.*, **46**, 2583–2604.
- 597 Toggweiler, J. R., and B. Samuels, 1993: Is the magnitude of the deep outflow from the Atlantic
598 Ocean actually governed by Southern Hemisphere winds? *The Global Carbon Cycle, NATO*
599 *ASI Ser., Ser. I*, M. Heimann, Ed., Springer, New York, 333–366.
- 600 Toggweiler, J. R., and B. Samuels, 1995: Effect of Drake Passage on the global thermohaline
601 circulation. *Deep Sea Res. I*, **42 (4)**, 477–500.
- 602 Toulany, B., and C. Garrett, 1984: Geostrophic control of fluctuating barotropic flow through
603 straits. *J. Phys. Oceanogr.*, **14**, 649–655.
- 604 Wolfe, C. L., and P. Cessi, 2010: What sets the strength of the mid-depth stratification and
605 overturning circulation in eddying ocean models? *J. Phys. Oceanogr.*, **40 (7)**, 1520–1538,
606 doi:10.1175/2010JPO4393.1.
- 607 Woodgate, R. A., 2018: Increases in the Pacific inflow to the Arctic from 1990 to 2015, and insights
608 into seasonal trends and driving mechanisms from year-round Bering Strait mooring data. *Prog.*
609 *Oceanogr.*, **160**, 124–154.

- 610 Young, W. R., 2012: An exact thickness-weighted average formulation of the Boussinesq equations.
611 *J. Phys. Oceanogr.*, **42** (5), 692–707.
- 612 Zhang, J., R. Woodgate, and R. Moritz, 2010: Sea ice response to atmospheric and oceanic forcing
613 in the Bering Sea. *J. Phys. Oceanogr.*, **40**, 1729–1747.

614 **LIST OF TABLES**

615 **Table 1.** Standard values of the parameters used in the conceptual model of (12) and (13). . 31

Parameter	Value	Notes
θ_s	30°S	Latitude of tip of Eurafrikan continent
θ_c	52°S	Latitude of subpolar/subtropical intergyre boundary
f_s	$-7.3 \times 10^{-5} s^{-1}$	Coriolis parameter at θ_s
f_c	$-9.9 \times 10^{-5} s^{-1}$	Coriolis parameter at θ_c
f_{BS}	$1.2 \times 10^{-4} s^{-1}$	Coriolis parameter at Bering Strait
τ_s	$4.3 \times 10^{-2} Pa$	Wind-stress at θ_s
τ_c	$0.2 Pa$	Wind-stress at θ_c
L_p	$1.3 \times 10^7 m$	Width of the wide basin at θ_s
L	$1.7 \times 10^7 m$	Width of the Southern circumpolar basin at θ_c
L_c	$3.1 \times 10^6 m$	Distance between θ_c and h outcrop in Southern Ocean
L_s	$4.4 \times 10^6 m$	Distance between θ_s and h outcrop in Southern Ocean
A_a	$8.8 \times 10^{13} m^2$	Area of the narrow basin
A_p	$1.4 \times 10^{14} m^2$	Area of the wide basin
H_{BS}	67m	Mean depth of the Bering strait
ρ_o	$1000 kg m^{-3}$	Boussinesq reference density
κ	$2 \times 10^{-5} m^2 s^{-1}$	Diapycnal diffusivity
κ_{GM}	$500 m^2 s^{-1}$	Coefficient of eddy parametrization
g'	$5.9 \times 10^{-3} m s^{-2}$	Reduced gravity

TABLE 1. Standard values of the parameters used in the conceptual model of (12) and (13).

616 **LIST OF FIGURES**

617 **Fig. 1.** Time-averaged sea-level (SSH) anomaly from Estimating the Circulation and Climate of the
618 Ocean (version 4, release 3) (ECCO4 henceforth) (Forget et al. 2015; Fukumori et al. 2017).
619 The left panel shows a polar view, and the right panel shows a Mercator-projection global
620 view. The colorbar is the same for the two panels and the units are in m. 34

621 **Fig. 2.** Geometry of the conceptual model illustrating the buoyancy budget for the residual circulation
622 above the isopycnal separating the upper and lower limb of the mid-depth MOC when sinking
623 is in the Atlantic-like (narrow) basin. Top panel: 3-D view. Bottom panel: 2-D view showing
624 the latitudes of solid boundaries. Pressure and SSH are constant along the segments B-C
625 and D-E, and equal to the values at point B and E respectively. 35

626 **Fig. 3.** Same as figure 2 except that sinking is in the Pacific-like (wide) basin. 36

627 **Fig. 4.** Approximate (dashed) and numerical (solid) solutions of the system (16-17) for the parameter
628 values given in table 1. 37

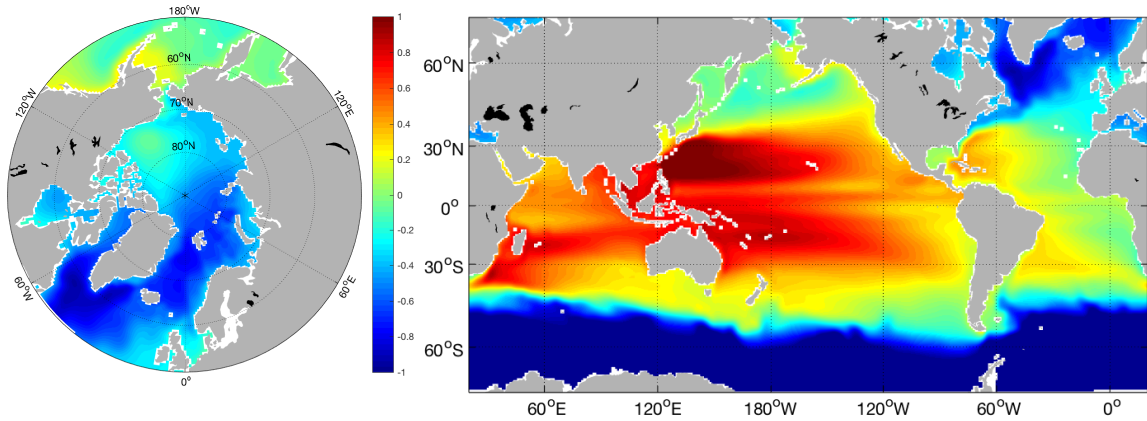
629 **Fig. 5.** The transport across the strait using (7) with h_p obtained from the numerical solution of the
630 system (16-17) for the parameter values given in table 1 (solid line). The star markers show
631 the transport across the strait for the primitive equation computations (MITgcm) for different
632 widths of the strait and amplitude of the westerly wind-stress maximum in the Southern
633 Hemisphere. 38

634 **Fig. 6.** Top panel: Sea surface height (in m) for a computation with sinking in the narrow basin
635 (“2 winds” surface wind-stress and “Narrow salty - Wide fresh” freshwater flux in figure 7).
636 Bottom panel: Sea surface height (in m) for a computation with sinking in the wide basin
637 (“2 winds” surface wind-stress and “Wide salty - Narrow fresh” freshwater flux in figure 7).
638 In both panels the solid boundaries are denoted by gray color, and the Bering Strait is 272km
639 wide (double strait). Notice that SSH is lower in the sinking basin relative to the non-sinking
640 basin. The westernmost 20° of longitude are repeated on the eastern side of the domain to
641 illustrate the 210° periodicity in longitude. 39

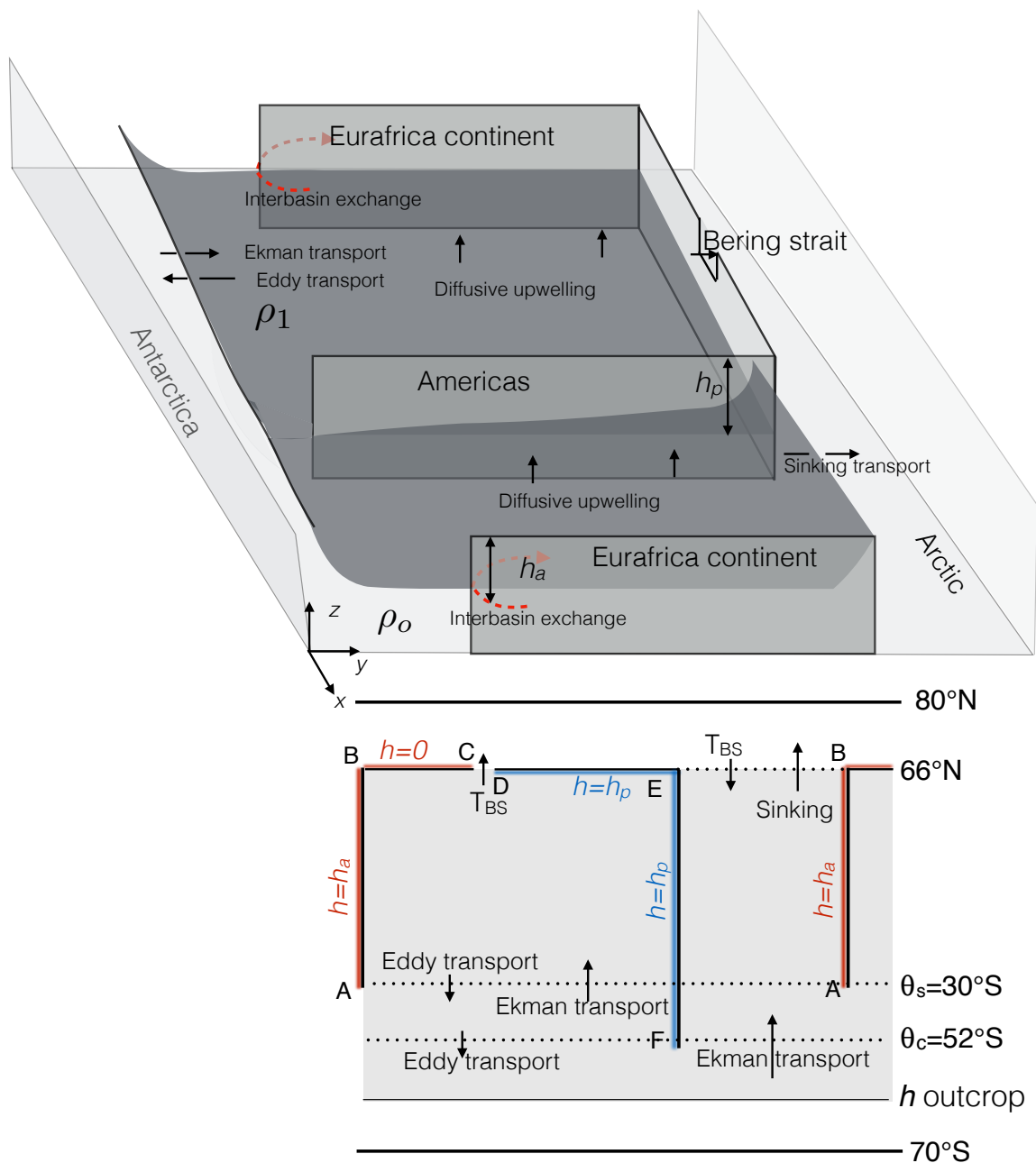
642 **Fig. 7.** Top panel: the different surface wind-stresses profiles applied to the MITgcm. Middle panel:
643 relaxation temperature, T^* , to which the model surface temperature is relaxed on a time-scale
644 of 15 days. Bottom panel: the negative surface freshwater flux. The salinity (virtual) flux
645 profiles imposed at the model’s surface is the negative of the freshwater flux, multiplied by
646 the reference salinity (35 PSU). The black lines show the profiles for sinking in the narrow
647 sector (Atlantic-like): the profile in the narrow sector (0°E to 70°E) (black solid) and in
648 the wide sector (140°W to 0°E) (black dashed), amounting to a 0.13Sv difference of area-
649 integrated freshwater flux between the two sectors (wide minus narrow). The blue lines show
650 the profiles for sinking in the wide sector (Pacific-like): the profile in the narrow sector (0°E
651 to 70°E) (blue dashed) and in the wide sector (140°W to 0°E) (blue solid), amounting to a
652 -0.58Sv difference of area integrated freshwater flux between the two sectors (wide minus
653 narrow). 40

654 **Fig. 8.** Time-averaged density anomaly (density -1000 kg/m³) at the longitude of the eastern bound-
655 ary of the narrow basin as a function of latitude and depth. The magenta vertical line denotes
656 the southern tip of the long continent, the yellow line is the southern tip of the short continent
657 and the white dashed line is the latitude of the strait. The top left panel is forced by the
658 wind stress with the black profile (“1 winds”) in figure 7, the top right panel by the “2
659 winds” profile, and the bottom left panel by the “3 winds” profile. These three panels are
660 all forced by the freshwater flux marked by black lines in figure 7 (“Wide fresh – Narrow

661	salty”), which induces sinking in the narrow basin. The bottom right panel is forced by the	
662	“2 winds” wind-stress, and by the freshwater flux marked by blue lines in figure 7 (“Wide	
663	salty – Narrow fresh”), which induces sinking in the wide basin. The contour interval is	
664	0.3 kg/m ³ . The thick contour denotes the isopycnal approximately separating the upper and	
665	lower limbs of the MOC, i.e. the “separating depth”.	41
666	Fig. 9. Same as figure 8, but for the density on the eastern boundary of the wide basin. Here there	
667	is a solid boundary at the latitude of the strait marked by a thick white vertical line.	42
668	Fig. 10. Time and zonally averaged residual streamfunction in the narrow basin as a function of	
669	latitude and depth. The magenta vertical line denotes the southern tip of the long continent,	
670	the yellow line is the southern tip of the short continent and the white dashed line is the	
671	latitude of the strait. The top left panel is forced by the wind stress with the black profile (“1	
672	winds”) in figure 7, the top right panel by the “2 winds” profile, and the bottom left panel	
673	by the “3 winds” profile. These three panels are all forced by the freshwater flux marked by	
674	black lines in figure 7 (“Wide fresh – Narrow salty”), which induces sinking in the narrow	
675	basin. The bottom right panel is forced by the “2 winds” wind-stress, and by the (“Wide	
676	salty – Narrow fresh”) freshwater flux, which induces sinking in the wide basin. The contour	
677	interval is 2Sv.	43
678	Fig. 11. Same as figure 10, but for the residual streamfunction in the wide basin. The time-averaged	
679	transport across the strait in Sv , T_{BS} , is marked in the bottom right section of each contour plot.	44
680	Fig. 12. SSH along the arclengths following the anticlockwise path along the eastern and northern	
681	boundaries of the wide basin (solid lines and upper abscissa labels), and the clockwise path	
682	along the eastern boundary of the narrow basin and the northern boundary of the wide basin	
683	(dashed lines and lower abscissa labels). Along the northern boundary of the wide-basin,	
684	the path is one-grid point south of the strait’s latitude, while for the narrow basin the path is	
685	evaluated one-grid point north of the strait’s latitude. The capital letters denote the landmark	
686	points marked in the lower panel of figure 2. The colors of the lines indicate the strength	
687	of the wind-stress in the Southern Hemisphere circumpolar region, using the same color	
688	scheme as in the upper panel of figure 7.	45
689	Fig. 13. Time and zonally averaged residual streamfunction in the narrow basin as a function of	
690	latitude and depth. The magenta vertical line denotes the southern tip of the long continent,	
691	the yellow line is the southern tip of the short continent and the white dashed line is the	
692	latitude of the strait. The bottom right panel has a closed strait, the bottom left panel has a	
693	136km strait (“single strait”), the top left panel has a strait 272 km wide (“double strait”),	
694	the top right panel a strait 408km . All panels are forced by the wind-stress in the red profile	
695	(“2 winds”) and the freshwater flux marked by black lines in figure 7 (“Wide fresh – Narrow	
696	salty”), which induces sinking in the narrow basin. The contour interval is 2Sv.	46
697	Fig. 14. Same as figure 10, but for the residual streamfunction in the wide basin. The time-averaged	
698	transport across the strait in Sv , T_{BS} , is marked in the bottom right section of each contour plot.	47



699 FIG. 1. Time-averaged sea-level (SSH) anomaly from Estimating the Circulation and Climate of the Ocean
 700 (version 4, release 3) (ECCO4 henceforth) (Forget et al. 2015; Fukumori et al. 2017). The left panel shows a
 701 polar view, and the right panel shows a Mercator-projection global view. The colorbar is the same for the two
 702 panels and the units are in m.



703 FIG. 2. Geometry of the conceptual model illustrating the buoyancy budget for the residual circulation above
 704 the isopycnal separating the upper and lower limb of the mid-depth MOC when sinking is in the Atlantic-like
 705 (narrow) basin. Top panel: 3-D view. Bottom panel: 2-D view showing the latitudes of solid boundaries.
 706 Pressure and SSH are constant along the segments B-C and D-E, and equal to the values at point B and E
 707 respectively.

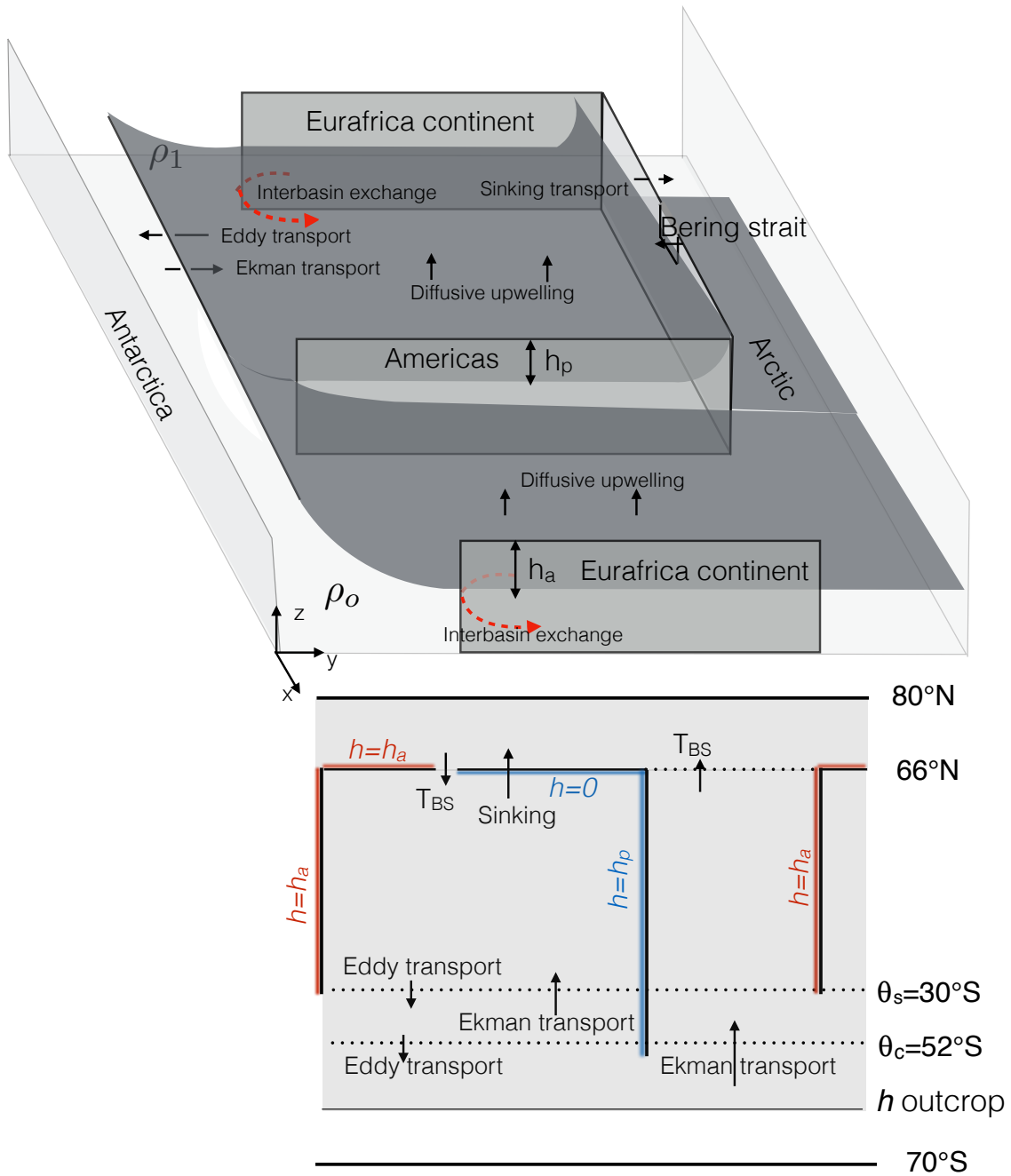
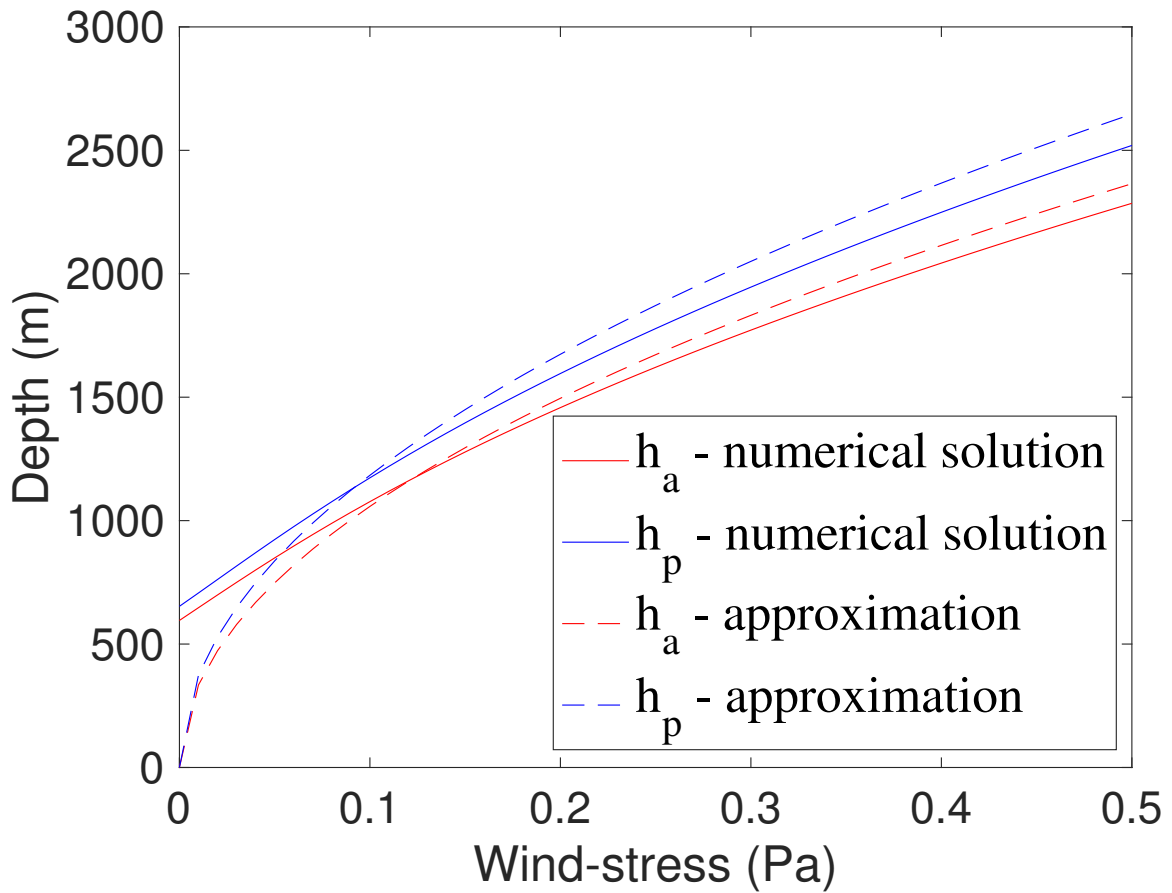
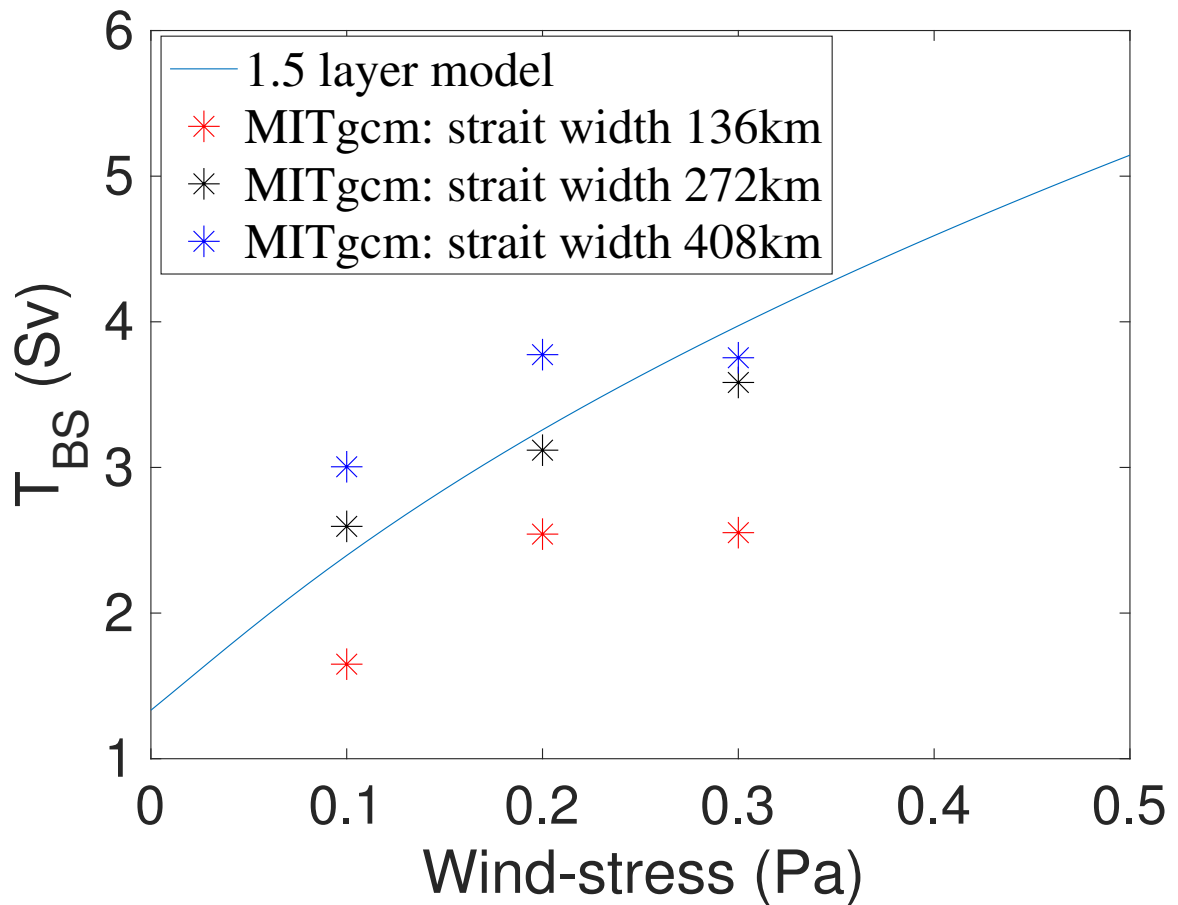


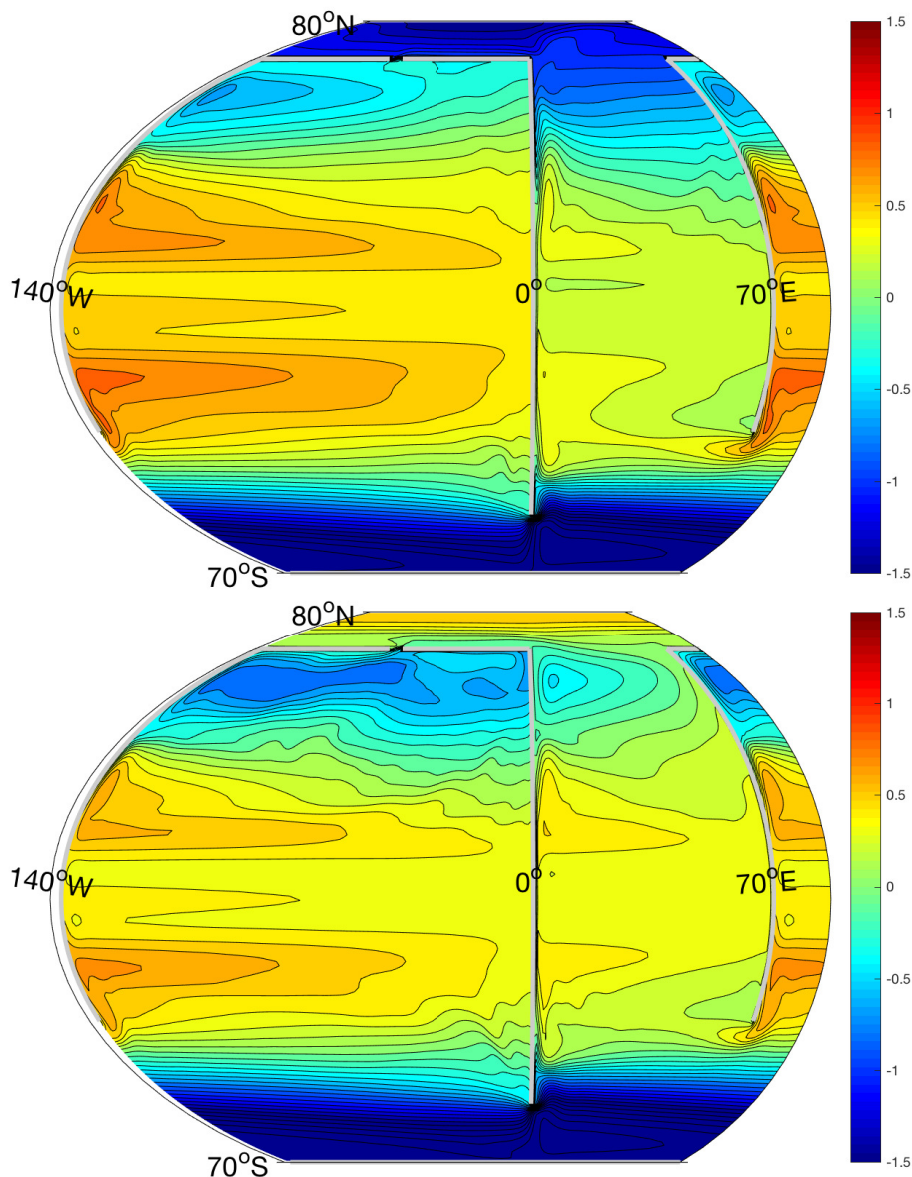
FIG. 3. Same as figure 2 except that sinking is in the Pacific-like (wide) basin.



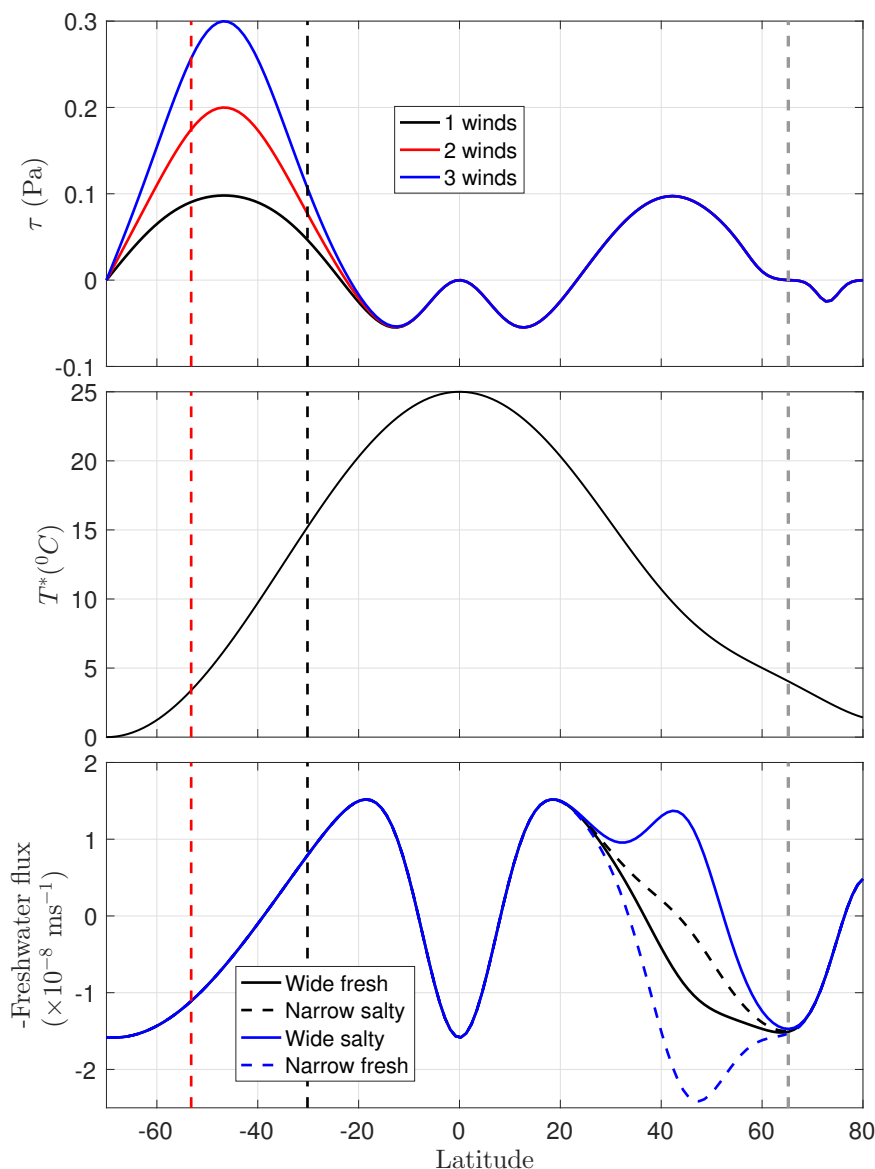
708 FIG. 4. Approximate (dashed) and numerical (solid) solutions of the system (16-17) for the parameter values
 709 given in table 1.



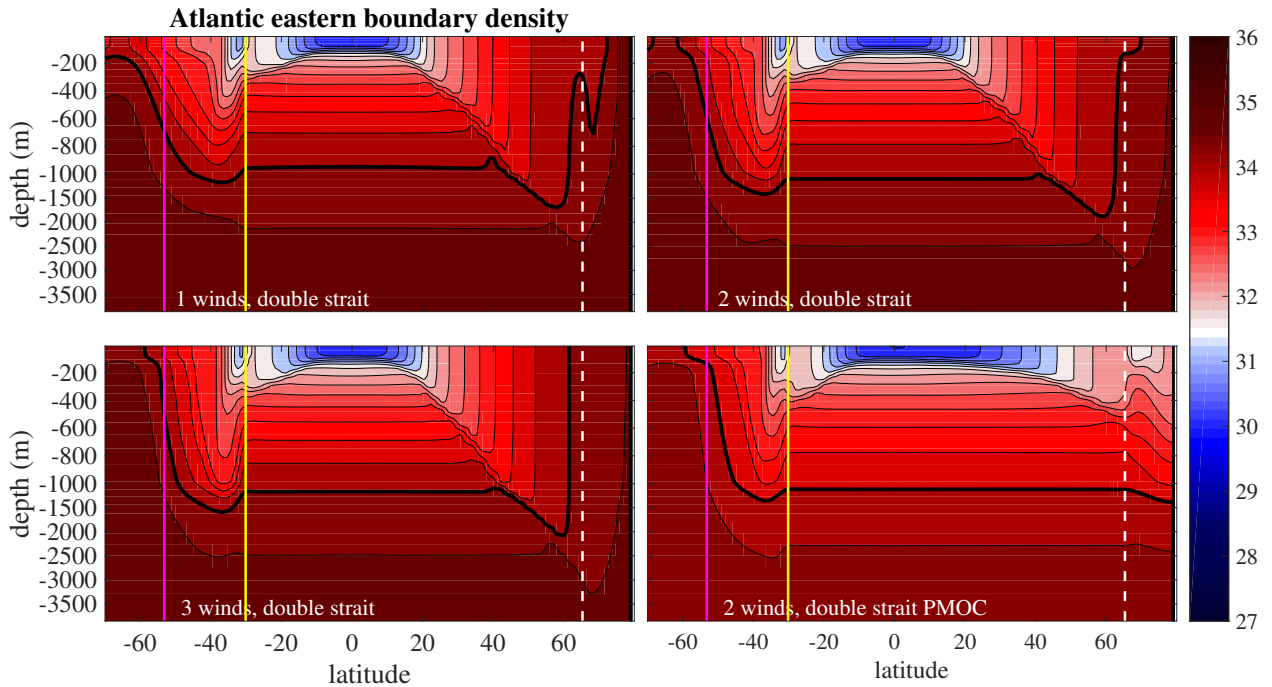
710 FIG. 5. The transport across the strait using (7) with h_p obtained from the numerical solution of the system
 711 (16-17) for the parameter values given in table 1 (solid line). The star markers show the transport across the strait
 712 for the primitive equation computations (MITgcm) for different widths of the strait and amplitude of the westerly
 713 wind-stress maximum in the Southern Hemisphere.



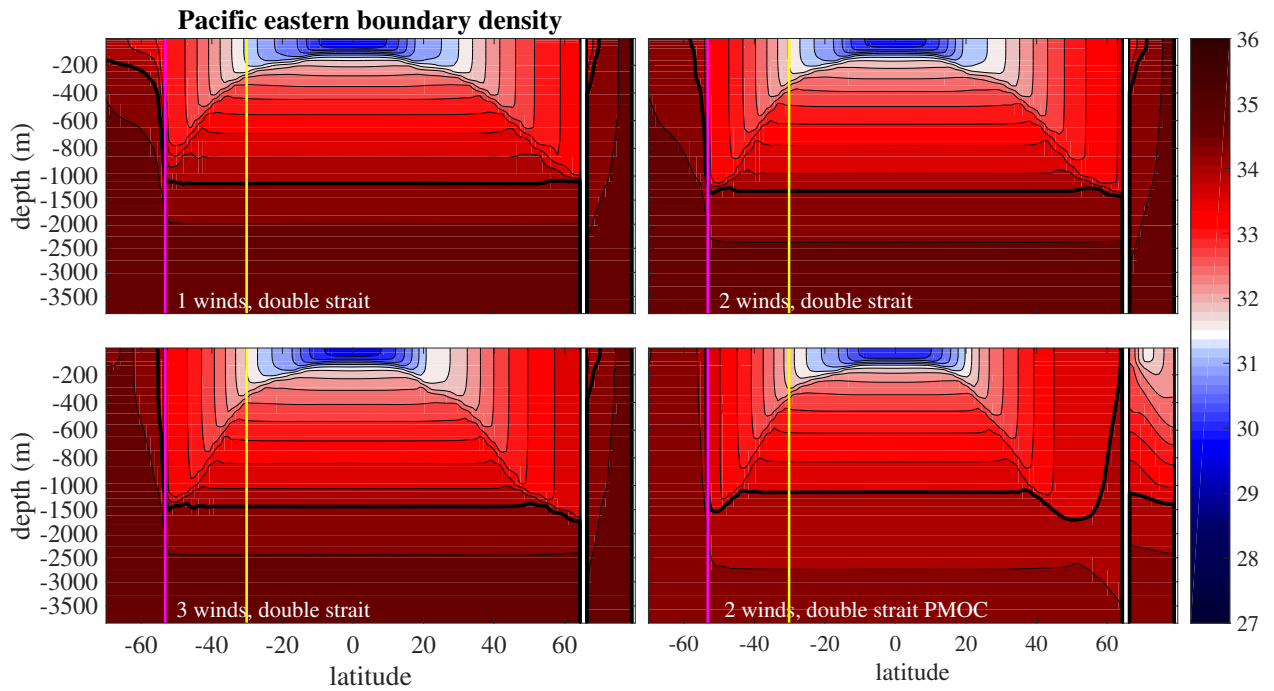
714 FIG. 6. Top panel: Sea surface height (in m) for a computation with sinking in the narrow basin (“2 winds”
 715 surface wind-stress and “Narrow salty - Wide fresh” freshwater flux in figure 7). Bottom panel: Sea surface
 716 height (in m) for a computation with sinking in the wide basin (“2 winds” surface wind-stress and “Wide salty
 717 - Narrow fresh” freshwater flux in figure 7). In both panels the solid boundaries are denoted by gray color, and
 718 the Bering Strait is 272km wide (double strait). Notice that SSH is lower in the sinking basin relative to the
 719 non-sinking basin. The westernmost 20° of longitude are repeated on the eastern side of the domain to illustrate
 720 the 210° periodicity in longitude.



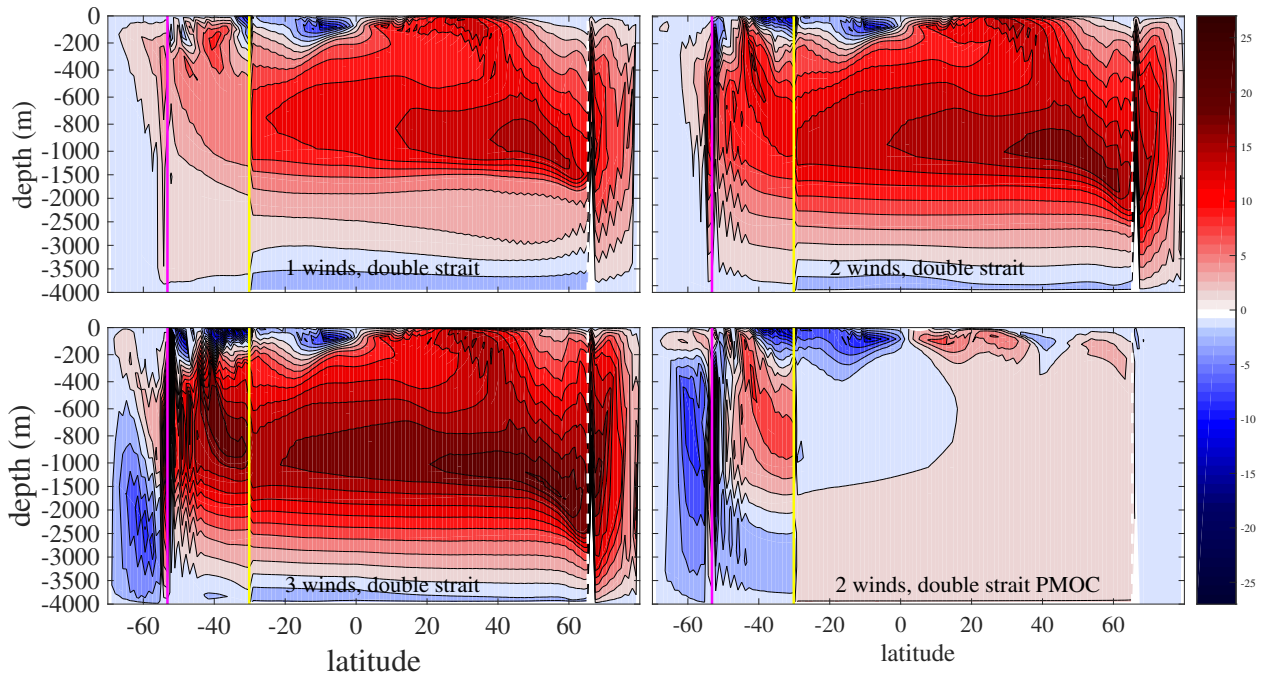
721 FIG. 7. Top panel: the different surface wind-stresses profiles applied to the MITgcm. Middle panel: relaxation
 722 temperature, T^* , to which the model surface temperature is relaxed on a time-scale of 15 days. Bottom panel:
 723 the negative surface freshwater flux. The salinity (virtual) flux profiles imposed at the model's surface is the
 724 negative of the freshwater flux, multiplied by the reference salinity (35 PSU). The black lines show the profiles
 725 for sinking in the narrow sector (Atlantic-like): the profile in the narrow sector (0°E to 70°E) (black solid) and in
 726 the wide sector (140°W to 0°E) (black dashed), amounting to a 0.13Sv difference of area-integrated freshwater
 727 flux between the two sectors (wide minus narrow). The blue lines show the profiles for sinking in the wide sector
 728 (Pacific-like): the profile in the narrow sector (0°E to 70°E) (blue dashed) and in the wide sector (140°W to 0°E)
 729 (blue solid), amounting to a -0.58Sv difference of area integrated freshwater flux between the two sectors (wide
 730 minus narrow).



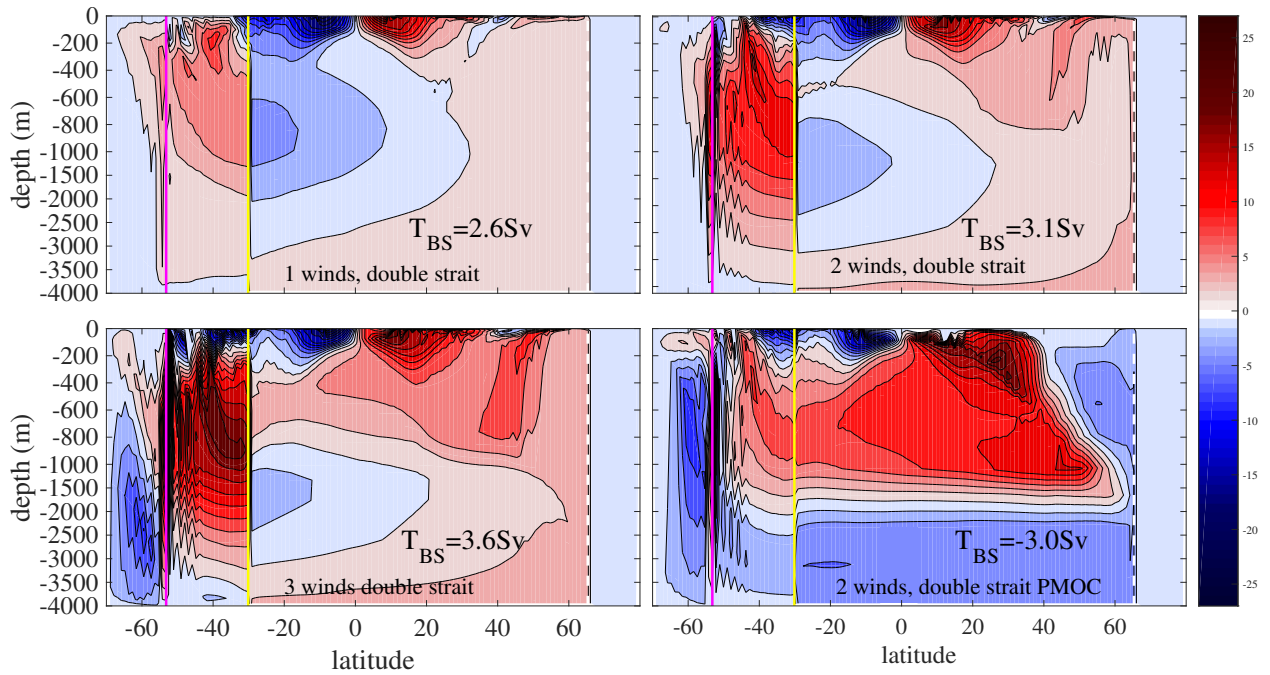
731 FIG. 8. Time-averaged density anomaly (density -1000 kg/m³) at the longitude of the eastern boundary of the
 732 narrow basin as a function of latitude and depth. The magenta vertical line denotes the southern tip of the long
 733 continent, the yellow line is the southern tip of the short continent and the white dashed line is the latitude of
 734 the strait. The top left panel is forced by the wind stress with the black profile (“1 winds”) in figure 7, the top
 735 right panel by the “2 winds” profile, and the bottom left panel by the “3 winds” profile. These three panels are
 736 all forced by the freshwater flux marked by black lines in figure 7 (“Wide fresh – Narrow salty”), which induces
 737 sinking in the narrow basin. The bottom right panel is forced by the “2 winds” wind-stress, and by the freshwater
 738 flux marked by blue lines in figure 7 (“Wide salty – Narrow fresh”), which induces sinking in the wide basin.
 739 The contour interval is 0.3 kg/m³. The thick contour denotes the isopycnal approximately separating the upper
 740 and lower limbs of the MOC, i.e. the “separating depth”.



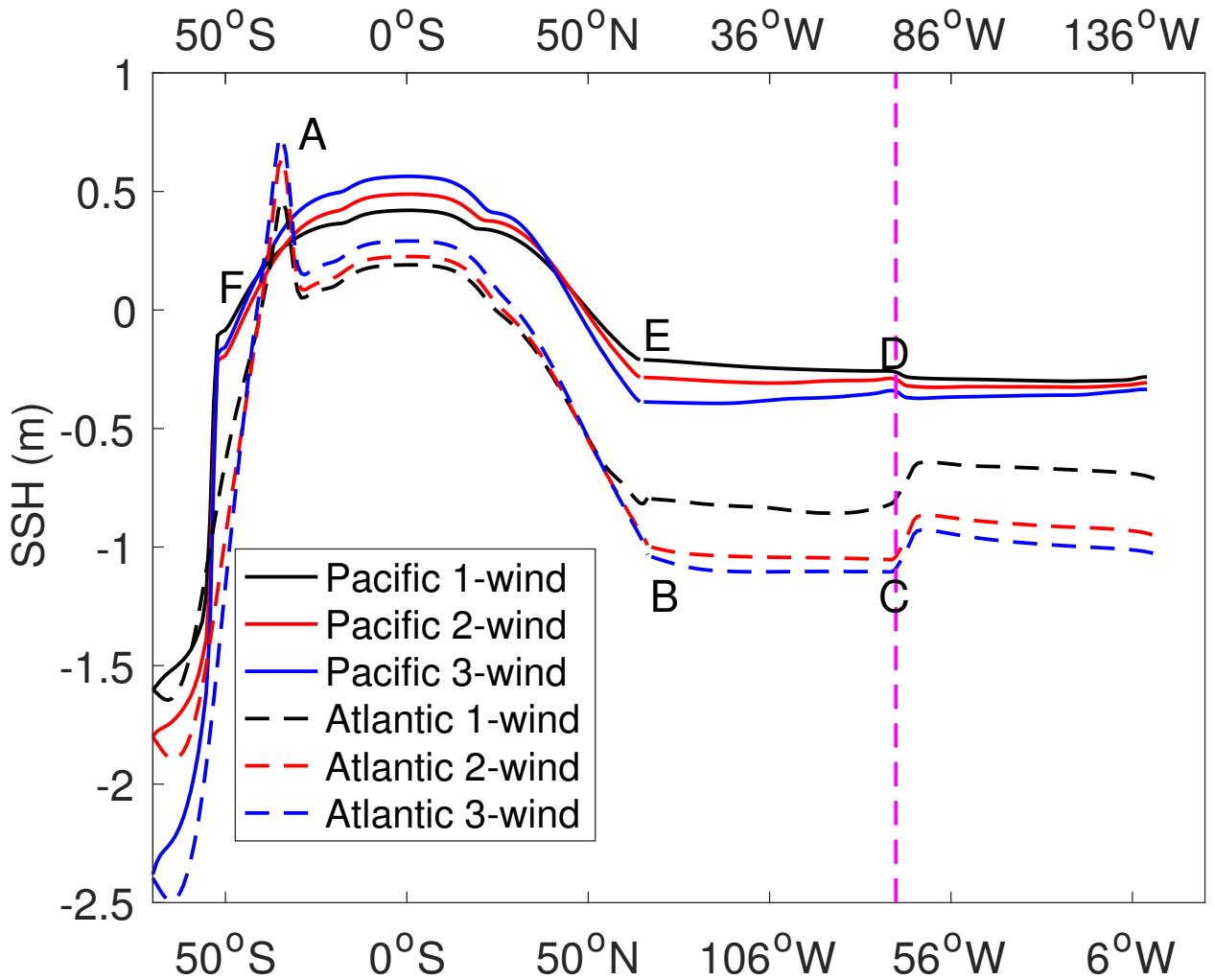
741 FIG. 9. Same as figure 8, but for the density on the eastern boundary of the wide basin. Here there is a solid
 742 boundary at the latitude of the strait marked by a thick white vertical line.



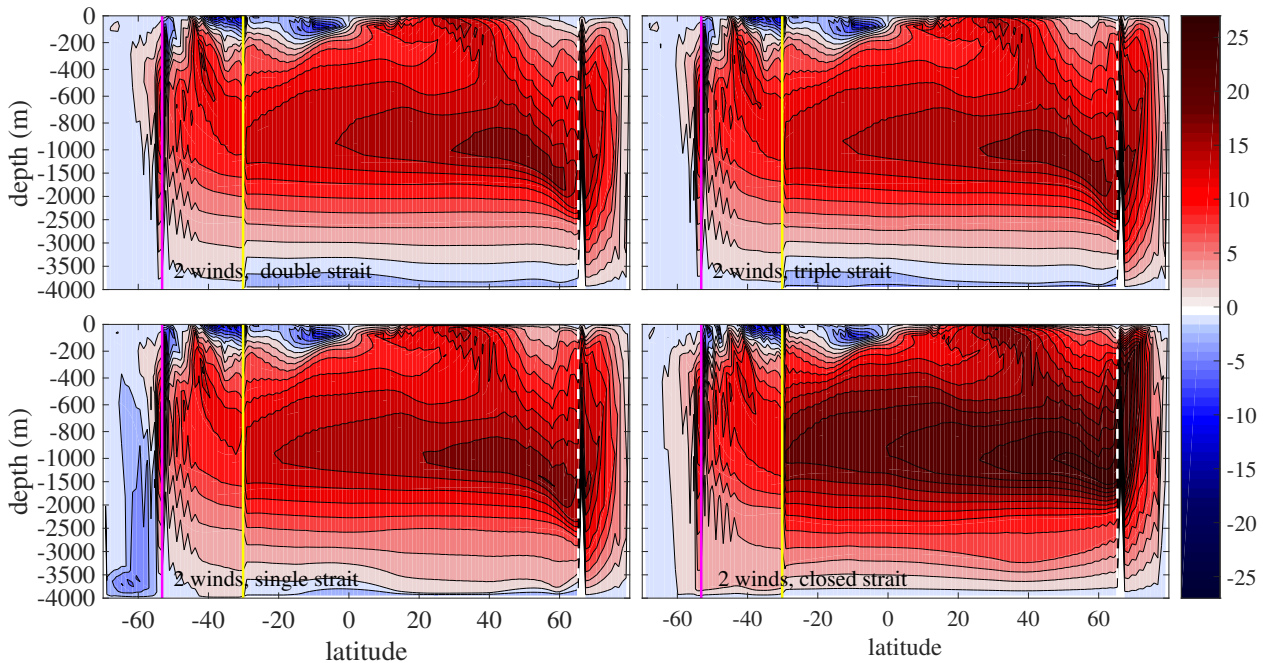
743 FIG. 10. Time and zonally averaged residual streamfunction in the narrow basin as a function of latitude and
 744 depth. The magenta vertical line denotes the southern tip of the long continent, the yellow line is the southern
 745 tip of the short continent and the white dashed line is the latitude of the strait. The top left panel is forced by the
 746 wind stress with the black profile (“1 winds”) in figure 7, the top right panel by the “2 winds” profile, and the
 747 bottom left panel by the “3 winds” profile. These three panels are all forced by the freshwater flux marked by
 748 black lines in figure 7 (“Wide fresh – Narrow salty”), which induces sinking in the narrow basin. The bottom
 749 right panel is forced by the “2 winds” wind-stress, and by the (“Wide salty – Narrow fresh”) freshwater flux,
 750 which induces sinking in the wide basin. The contour interval is 2Sv.



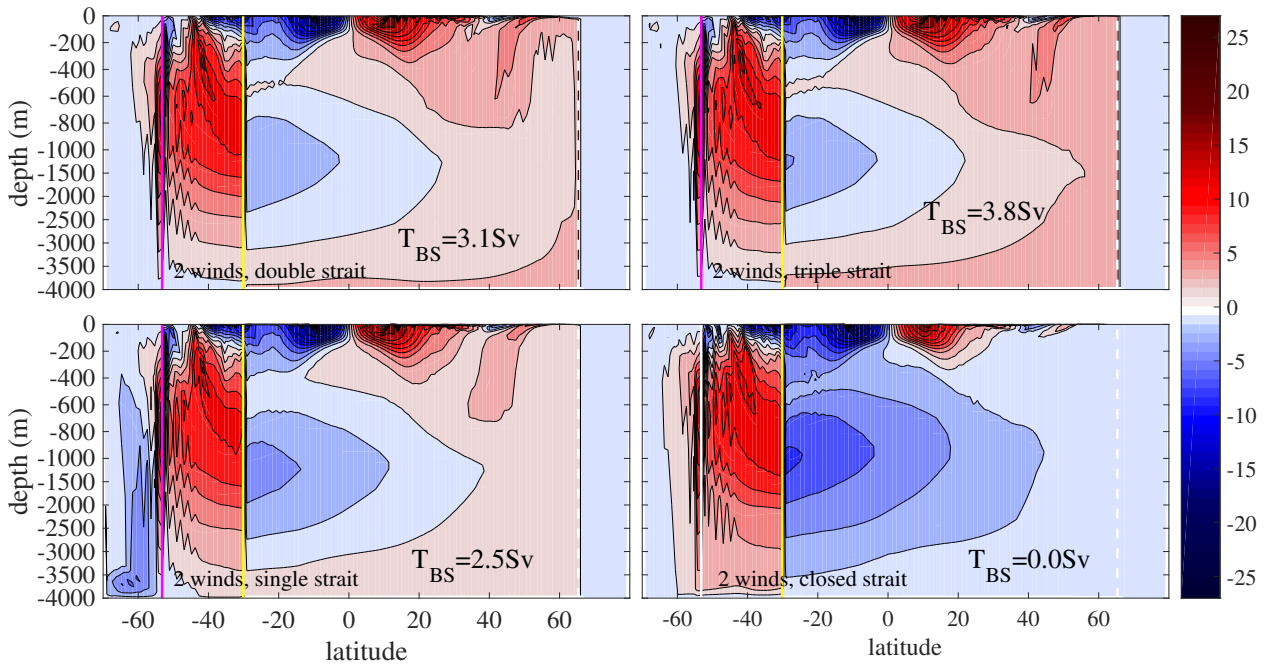
751 FIG. 11. Same as figure 10, but for the residual streamfunction in the wide basin. The time-averaged transport
 752 across the strait in Sv, T_{BS} , is marked in the bottom right section of each contour plot.



753 FIG. 12. SSH along the arclengths following the anticlockwise path along the eastern and northern boundaries
 754 of the wide basin (solid lines and upper abscissa labels), and the clockwise path along the eastern boundary of
 755 the narrow basin and the northern boundary of the wide basin (dashed lines and lower abscissa labels). Along the
 756 northern boundary of the wide-basin, the path is one-grid point south of the strait's latitude, while for the narrow
 757 basin the path is evaluated one-grid point north of the strait's latitude. The capital letters denote the landmark
 758 points marked in the lower panel of figure 2. The colors of the lines indicate the strength of the wind-stress in
 759 the Southern Hemisphere circumpolar region, using the same color scheme as in the upper panel of figure 7.



760 FIG. 13. Time and zonally averaged residual streamfunction in the narrow basin as a function of latitude and
 761 depth. The magenta vertical line denotes the southern tip of the long continent, the yellow line is the southern
 762 tip of the short continent and the white dashed line is the latitude of the strait. The bottom right panel has a
 763 closed strait, the bottom left panel has a 136km strait (“single strait”), the top left panel has a strait 272 km wide
 764 (“double strait”), the top right panel a strait 408km . All panels are forced by the wind-stress in the red profile (“2
 765 winds”) and the freshwater flux marked by black lines in figure 7 (“Wide fresh – Narrow salty”), which induces
 766 sinking in the narrow basin. The contour interval is 2Sv.



767 FIG. 14. Same as figure 10, but for the residual streamfunction in the wide basin. The time-averaged transport
 768 across the strait in Sv, T_{BS} , is marked in the bottom right section of each contour plot.